Article

Cell-programmed nutrient partitioning in the tumour microenvironment

Bradley I. Reinfeld[1,2,3,16], Matthew Z. Madden[1,4,16], Melissa M. Wolf[2,3], Anna Chytil[2], Jackie E. Bader[4], Andrew R. Patterson[4], Ayaka Sugiura[1,4], Allison S. Cohen[5,6], Ahmed Ali[7,8], Brian T. Do[7,8], Alexander Muir[9], Caroline A. Lewis[10], Rachel A. Hongo[2,4], Kirsten L. Young[2,4], Rachel E. Brown[1,2,3], Vera M. Todd[2,3], Tessa Huffstater[11], Abin Abraham[1,12], Richard T. O'Neil[2,13], Matthew H. Wilson[2,13], Fuxue Xin[5,6], M. Noor Tantawy[5,6], W. David Merryman[11], Rachelle W. Johnson[2], Christopher S. Williams[2,13], Emily F. Mason[4], Frank M. Mason[2], Katherine E. Beckermann[2], Matthew G. Vander Heiden[7,8,14], H. Charles Manning[5,6], Jeffrey C. Rathmell[4,15 ✉] & W. Kimryn Rathmell[2,15 ✉]

Cancer cells characteristically consume glucose through Warburg metabolism[1], a process that forms the basis of tumour imaging by positron emission tomography (PET). Tumour-infiltrating immune cells also rely on glucose, and impaired immune cell metabolism in the tumour microenvironment (TME) contributes to immune evasion by tumour cells[2–4]. However, whether the metabolism of immune cells is dysregulated in the TME by cell-intrinsic programs or by competition with cancer cells for limited nutrients remains unclear. Here we used PET tracers to measure the access to and uptake of glucose and glutamine by specific cell subsets in the TME. Notably, myeloid cells had the greatest capacity to take up intratumoral glucose, followed by T cells and cancer cells, across a range of cancer models. By contrast, cancer cells showed the highest uptake of glutamine. This distinct nutrient partitioning was programmed in a cell-intrinsic manner through mTORC1 signalling and the expression of genes related to the metabolism of glucose and glutamine. Inhibiting glutamine uptake enhanced glucose uptake across tumour-resident cell types, showing that glutamine metabolism suppresses glucose uptake without glucose being a limiting factor in the TME. Thus, cell-intrinsic programs drive the preferential acquisition of glucose and glutamine by immune and cancer cells, respectively. Cell-selective partitioning of these nutrients could be exploited to develop therapies and imaging strategies to enhance or monitor the metabolic programs and activities of specific cell populations in the TME.

The founding observation in cancer metabolism was that tumours consume glucose to produce lactate in the presence of oxygen[1]. Aerobic glycolysis is widely observed in rapidly proliferating cells, including activated immune cells, to support biosynthetic demands[1]. In vivo carbon-labelling studies have confirmed that glucose supports anabolic metabolism in transformed cells and T cells[5,6]. Glutamine metabolism provides anaplerotic fuel, and restrains glucose-dependent differentiation and the function of macrophages and T cells[7–9]. These metabolic pathways may become disrupted in immune cells in the TME to prevent anti-tumour immunity[2–4,10].

Glucose uptake can be measured using ^{18}F-fluorodeoxyglucose (FDG) PET imaging to detect cancers and monitor therapeutic responses. Depletion of glucose in the TME by cancer cells may drive nutrient competition as a metabolic mechanism of immunosuppression[3,4]. High concentrations of glucose, ranging from 0.2 to 2 mM, have been measured in the TME in mice and humans[2,11,12]. Furthermore, the metabolic phenotypes of T cells can persist even after these cells are removed from the TME and cultured in nutrient-replete media[2,13]. The extent of intrinsic metabolic programming or nutrient competition for limited nutrients between cancer cells and immune cells remains uncertain. Here we used PET probes to directly measure the uptake of glucose and glutamine in cell subsets in the TME.

Nutrients partition in the TME

Immune cells may contribute substantially to glucose consumption in the TME. We measured nutrient abundance in the tissue interstitial fluid

[1]Medical Scientist Training Program, Vanderbilt University, Nashville, TN, USA. [2]Department of Medicine, Vanderbilt University Medical Center (VUMC), Nashville, TN, USA. [3]Graduate Program in Cancer Biology, Vanderbilt University, Nashville, TN, USA. [4]Department of Pathology, Microbiology and Immunology, VUMC, Nashville, TN, USA. [5]Department of Radiology and Radiological Sciences, VUMC, Nashville, TN, USA. [6]Vanderbilt University Institute of Imaging Science, VUMC, Nashville, TN, USA. [7]Koch Institute for Integrative Cancer Research and Department of Biology, Massachusetts Institute of Technology (MIT), Cambridge, MA, USA. [8]Broad Institute of MIT and Harvard University, Cambridge, MA, USA. [9]Ben May Department for Cancer Research, University of Chicago, Chicago, IL, USA. [10]Whitehead Institute for Biomedical Research, MIT, Cambridge, MA, USA. [11]Department of Biomedical Engineering, Vanderbilt University, Nashville, TN, USA. [12]Vanderbilt Genetics Institute, VUMC, Nashville, TN, USA. [13]Department of Veterans Affairs, Tennessee Valley Health System, Nashville, TN, USA. [14]Dana-Farber Cancer Institute, Boston, MA, USA. [15]Vanderbilt Center for Immunobiology and Vanderbilt-Ingram Cancer Center, VUMC, Nashville, TN, USA. [16]These authors contributed equally: Bradley I. Reinfeld, Matthew Z. Madden. ✉e-mail: jeff.rathmell@vumc.org; kimryn.rathmell@vumc.org
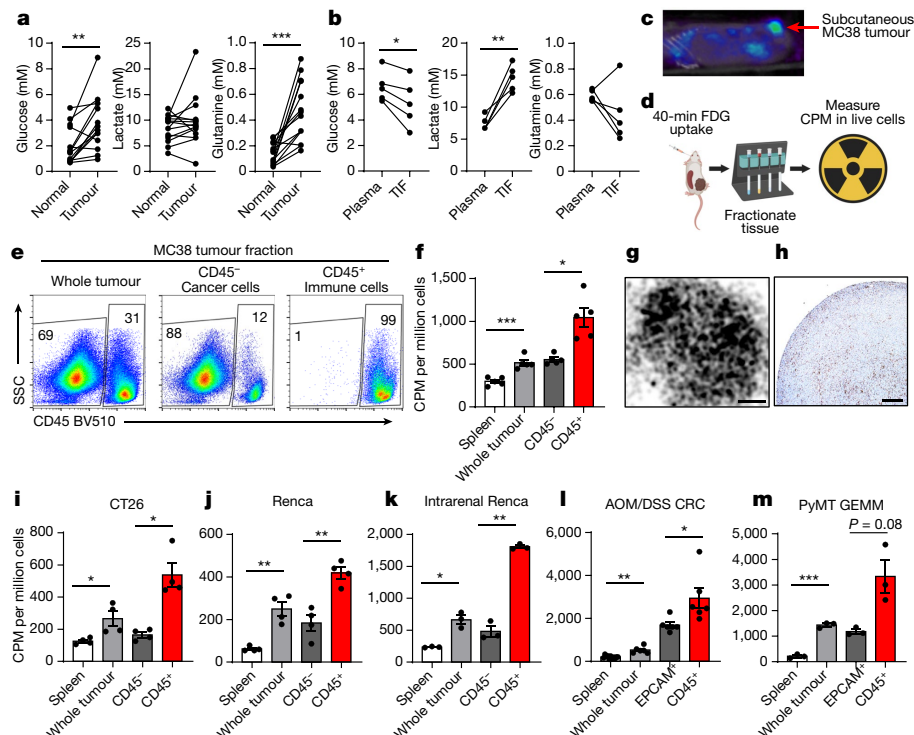
Fig. 1 | Glucose is preferentially consumed by immune cells over cancer cells. a, **b**, Quantification of interstitial fluid metabolites from human ccRCC tumours and matched adjacent healthy kidney tissue ($n = 14$ patients) (**a**) and mouse MC38 subcutaneous tumour interstitial fluid (TIF) and matched plasma ($n = 5$ mice) (**b**). **c**, Representative FDG PET image of an MC38 tumour (representative of $n > 20$ mice). **d**, Experimental schema. CPM, counts per minute. **e**, Representative flow cytometry analysis of MC38 whole tumour, CD45^{+}, and CD45^{−} cell fractions gated on live cells. **f**, FDG avidity in designated cell fractions from MC38 tumours ($n = 5$ mice). **g**, Representative (of $n = 3$ mice) tissue FDG autoradiography of an MC38 tumour. Scale bar, 800 μm.

h, Representative (of $n = 5$ mice) immunohistochemistry (IHC) for CD45 in an MC38 tumour. Scale bar, 200 μm. **i**–**m**, FDG avidity in designated tumour cell fractions from subcutaneous CT26 tumours (**i**; $n = 4$ mice) and Renca tumours (**j**; $n = 4$ mice); intrarenal Renca tumours (**k**; $n = 3$ mice); AOM/DSS colorectal cancer (CRC) tumours (**l**; $n = 6$ mice for tumour; $n = 11$ mice for spleen); and PyMT GEMM tumours (**m**; $n = 3$ mice). Each data point represents a biological replicate; data are mean ± s.e.m. Data in **b**, **c**, **e**–**m** are from representative studies performed independently at least twice. P values were calculated using a paired two-tailed t-test (**a**, **b**) or Welch's two-tailed t-test (**f**, **i**–**m**); *$P < 0.05$, **$P < 0.01$, ***$P < 0.001$; exact P values are provided in the Source Data.

from freshly resected specimens of human renal cell carcinoma (RCC) and mouse subcutaneous MC38 tumours using mass spectrometry[11] (Fig. 1a, b, Supplementary Table 1). Glucose, glutamine and lactate were all detectable in the TME at similar concentrations to those in matched healthy kidney tissue or plasma. We next directly measured in vivo glucose uptake to quantify the accessibility of glucose to distinct cell populations in the TME. Subcutaneous MC38 tumours were visualized by FDG PET imaging and per-cell in vivo ^{18}F radioactivity was measured in fractionated tumour cell subsets (Fig. 1c, d). Magnetic microbeads for CD45^{+} selection fractionated tumour cells into enriched CD45^{−} (predominantly cancer cell) and CD45^{+} (immune cell) populations (Fig. 1e, Extended Data Fig. 1a). Unfractionated tumour cells exhibited a higher avidity for FDG than control tissue splenocytes (Fig. 1f). Notably, tumour-infiltrating CD45^{+} immune cells had a greater uptake of FDG per cell than did CD45^{−} cells. FDG autoradiography and immunohistochemistry revealed a homogenous distribution of FDG and CD45^{+} cells, showing that the differential uptake was not due to spatial distribution favouring immune cells (Fig. 1g, h). Immune cells also had a higher FDG avidity in mouse subcutaneous CT26 and renal carcinoma (Renca) tumours (Fig. 1i, j, Extended Data Fig. 1b, c), and orthotopic Renca tumours showed a higher per-cell FDG avidity in immune cells as compared to CD45^{−} tumour cells (Fig. 1k, Extended Data Fig. 1d). Infiltrating immune cells had a higher uptake of FDG than EPCAM^{+} cancer cells in both an azoxymethane and dextran sodium sulfate-induced (AOM/DSS) mouse model of inflammatory colon cancer and a Polyoma virus middle T antigen (PyMT) genetically engineered mouse model (GEMM) of breast cancer (Fig. 1l, m, Extended Data Fig. 1e–g). These

results show that glucose is available in the TME and preferentially partitions into infiltrating immune cells more so than into cancer cells across multiple models.

We used several different strategies to validate that this approach accurately measures the per-cell uptake of glucose in vivo. Immune cells isolated from MC38 tumours were confirmed to be tumour-infiltrating on the basis of minimal labelling after intravenous administration of a fluorescent anti-CD45 antibody that efficiently labelled immune cells in the blood and spleen (Extended Data Fig. 2a). FDG uptake had a dynamic range with a multiple-log scale of linearity (Extended Data Fig. 2b) and was independent of sample viability, cell yield and tumour mass across biological replicates and tumour models (Extended Data Fig. 2c). To confirm that FDG uptake did not occur during tumour processing, unlabelled single-cell suspensions of MC38 tumours were incubated with supernatants from FDG-labelled tumours. Ex vivo FDG uptake did not substantially contribute to the final FDG signal (Extended Data Fig. 2d, e). Finally, to specifically examine cancer cells apart from other CD45^{−} cells, THY1.1^{+} MC38 cells were implanted in THY1.1^{−} hosts and isolated using microbeads for THY1.1^{+} selection. Negatively selected THY1.1^{−} immune cells showed a higher FDG avidity than THY1.1^{+} cancer cells (Extended Data Fig. 2f–h). This approach thus specifically and quantitatively measures the in vivo glucose uptake of cancer and immune cells in the TME. We also tested the fluorescent glucose analogue 2-NBDG (2-[N-(7-nitrobenz-2-oxa-1,3-diazol-4-yl)amino]-2-deoxyglucose). Consistent with other in vitro findings[14], 2-NBDG was not specific for glucose uptake in vivo and comparative measures of radioactive FDG and 2-NBDG uptake in T cells from mice co-injected with both tracers
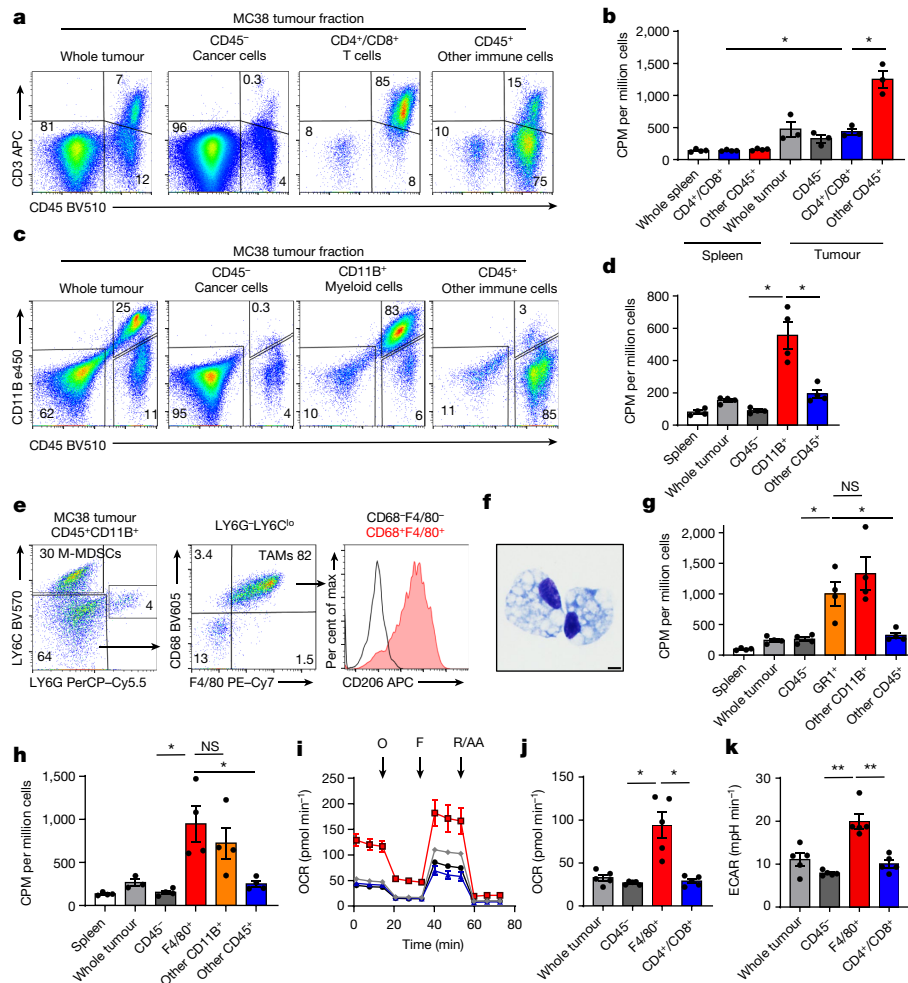
Fig. 2 | TME myeloid cells take up more glucose than cancer cells.
a, Representative flow cytometry from CD4$^+$ and CD8$^+$ (CD4$^+$/CD8$^+$) microbead-fractionated MC38 tumours gated on live cells. **b**, FDG avidity in designated cell fractions ($n = 3$ mice for tumour; $n = 4$ mice for spleen). **c**, Representative flow cytometry from CD11B$^+$ microbead-fractionated MC38 tumours gated on live cells. **d**, FDG avidity in designated cell fractions ($n = 4$ mice). **e**, Representative flow cytometry plots of MC38 tumour CD11B$^+$ myeloid cells. **f**, Representative (of $n = 2$ mice) haematoxylin and eosin (H&E)-stained micrograph of F4/80$^+$ microbead-isolated TAMs. Scale bar, 5 μm. **g, h**, FDG avidity in designated MC38 tumour cell fractions using GR1$^+$ microbeads

(g; $n = 4$ mice, except whole tumour, $n = 3$ mice) or F4/80$^+$ microbeads (**h**; $n = 4$ mice). **i**, Representative (of $n = 5$ mice) OCR tracings from MC38 tumour cell fractions with oligomycin (O), FCCP (F) or rotenone and antimycin A (R/AA). **j, k**, Basal mitochondrial OCR (**j**) and basal cellular ECAR (**k**) of MC38 tumour fractions ($n = 5$ mice). Each data point represents a biological replicate, except for **i**, which shows technical replicates of a single biological replicate; data are mean ± s.e.m. Independent representative studies were performed at least twice. P values were calculated using Welch's two-tailed t-test; *$P < 0.05$, **$P < 0.01$, ***$P < 0.001$; NS, not significant; exact P values are provided in the Source Data.

showed no correlation of FDG radioactivity with 2-NBDG (Extended Data Fig. 3, Supplementary Fig. 1).

Myeloid cells take up the most glucose

Effector T cells and inflammatory myeloid cells both use glycolysis and are targets of immunotherapeutic strategies in the TME. CD3$^+$ T cells, CD11B$^+$ myeloid cells and F4/80$^+$ macrophages were abundant in MC38 tumours without clear differences in spatial distribution or proximity to CD31$^+$ endothelial cells that would suggest differential nutrient access (Extended Data Fig. 4). Characterization of immune infiltrates across several tumour models showed that they varied in their composition of immune cells (Extended Data Fig. 5). We next sought to compare the uptake of FDG between tumour T cells, myeloid cells and cancer cells in the MC38 model using microbeads to isolate each population. T cells in the TME had a greater in vivo FDG avidity than resting splenic T cells and a similar FDG avidity to cancer cells (Fig. 2a, b, Extended

Data Fig. 6a), suggesting that these cells are not deprived of glucose. The glucose uptake of T cells was substantially lower, however, than that of the remaining CD45$^+$ non-T cells.

To characterize the non-T cell CD45$^+$ cells, myeloid cells were isolated using microbeads for CD11B$^+$ selection (Fig. 2c, d, Extended Data Fig. 6b). Notably, CD11B$^+$ myeloid cells exhibited a higher uptake of FDG per cell than did cancer cells and other immune cells in MC38 tumours. Myeloid cells from CT26 tumours showed a similar phenotype (Extended Data Fig. 6c, d), consistent with previous reports[15,16]. Flow cytometry analysis of CD45$^+$ CD11B$^+$ cells from MC38 tumours identified two dominant cell populations: LY6G$^-$LY6C^{hi} cells, consistent with monocytic myeloid-derived suppressor cells (M-MDSCs); and LY6G$^-$LY6C^{lo}F4/80^{hi}CD68$^+$CD206^{hi} cells, consistent with tumour-associated macrophages (TAMs) (Fig. 2e). Isolated F4/80^{hi} cells had a histiocytic morphology (Fig. 2f), in line with their classification as TAMs. Both M-MDSCs that were isolated using microbeads for GR1$^+$ selection and TAMs that were isolated using microbeads
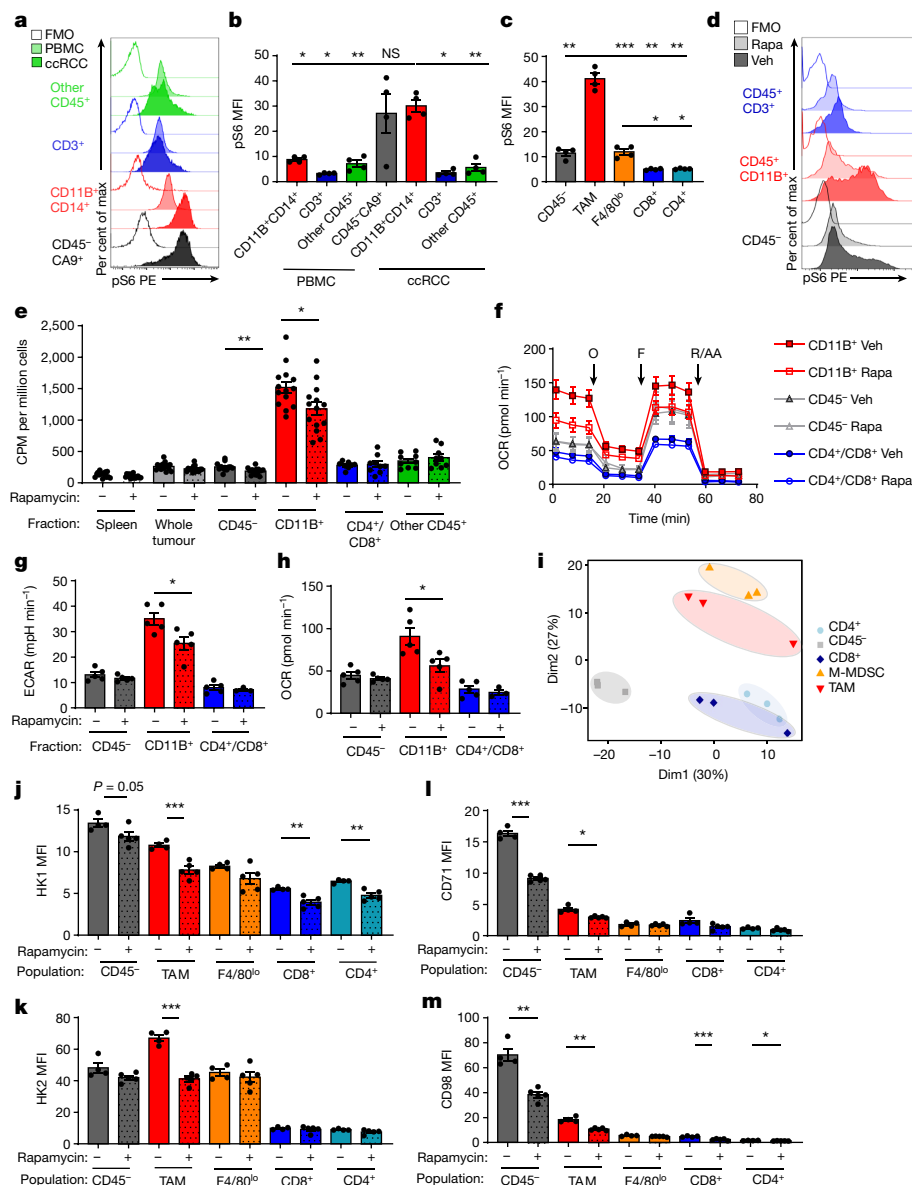
Fig. 3 | mTORC1 supports glucose uptake and metabolism in the TME.
a–**c**, Levels of pS6 in the indicated cell populations by flow cytometry in human peripheral blood mononuclear cells (PBMCs) and matched ccRCC tumours (**a**, representative histograms; **b**, quantification) ($n = 4$ patients) and in mouse MC38 tumours (**c**) ($n = 4$ mice). FMO, fluorescence minus one; MFI, median fluorescence intensity. **d**, Representative histograms of pS6 levels in MC38 tumour cells from mice treated with rapamycin (rapa) or vehicle (veh). **e**, FDG avidity in designated MC38 tumour cell fractions after treatment with rapamycin or vehicle ($n = 15$ mice for spleen vehicle; $n = 8$ mice for CD4$^+$/CD8$^+$ vehicle; $n = 9$ mice for CD4$^+$/CD8$^+$ rapamycin and other CD45$^+$; and $n = 14$ mice for all other groups). **f**, Representative (of $n = 5$ mice per group) OCR tracings from fractionated MC38 tumours from mice treated with rapamycin or vehicle with indicated injections of oligomycin, FCCP or and rotenone and antimycin A. **g**, **h**, Basal cellular ECAR (**g**) and basal mitochondrial OCR (**h**) of MC38 tumour fractions from mice treated with rapamycin or vehicle ($n = 5$ mice per group

except for CD4$^+$/CD8$^+$ rapamycin, $n = 3$ mice per group). **i**, PCA plot of metabolism-related mRNA transcripts from CD45$^-$, TAM, M-MDSC, CD8$^+$ T cell and CD4$^+$ T cell flow-sorted populations from MC38 tumours ($n = 3$ mice). Dim1, dimension 1; Dim2, dimension 2. **j**–**m**, Flow cytometry quantification of HK1 (**j**), HK2 (**k**), CD71 (**l**) and CD98 (**m**) in MC38 tumour cell populations from mice treated with rapamycin or vehicle ($n = 4$ mice for vehicle, $n = 5$ mice for rapamycin). Data in **c**, **d**, **i**–**m** are representative of at least two independent experiments; **e** represents the combined data of three independent experiments. Each data point represents a biological replicate except for **f**, which shows technical replicates of a single biological replicate; data are mean ± s.e.m. P values were calculated using the Brown-Forsythe and Welch ANOVA with Dunnett's T3 for multiple comparison tests (**b**, **c**) or Welch's two-tailed t-test (**e**–**m**); *$P < 0.05$, **$P < 0.01$, ***$P < 0.001$; exact P values are provided in the Source Data.

for F4/80$^+$ selection showed a high FDG avidity (Fig. 2g, h, Extended Data Fig. 6e, f). CD11B$^+$ cells exhibited a high uptake of glucose even in B cell- and T cell-deficient *Rag1$^{-/-}$* mice (Extended Data Fig. 5g), showing that high glucose uptake in myeloid cells is independent of adaptive immunity (Extended Data Fig. 6g). Conventional type 1 dendritic cells (cDC1) are critical for supporting anti-tumour activity in CD8$^+$ T cells[17]. CD11B$^-$CD11C$^+$ conventional dendritic cells—which exhibit a

MHCII$^+$CD103$^+$LY6C$^-$ phenotype, consistent with cDC1—had a glucose uptake that was lower than that of CD11B$^+$ myeloid cells but higher than that of cancer cells and non-myeloid immune cells in the TME (Extended Data Fig. 6h–j).

We conducted extracellular flux assays on microbead-fractionated MC38 tumours to validate the metabolic activity of cells in the TME. Isolated F4/80$^+$ TAMs maintained higher a basal cellular extracellular
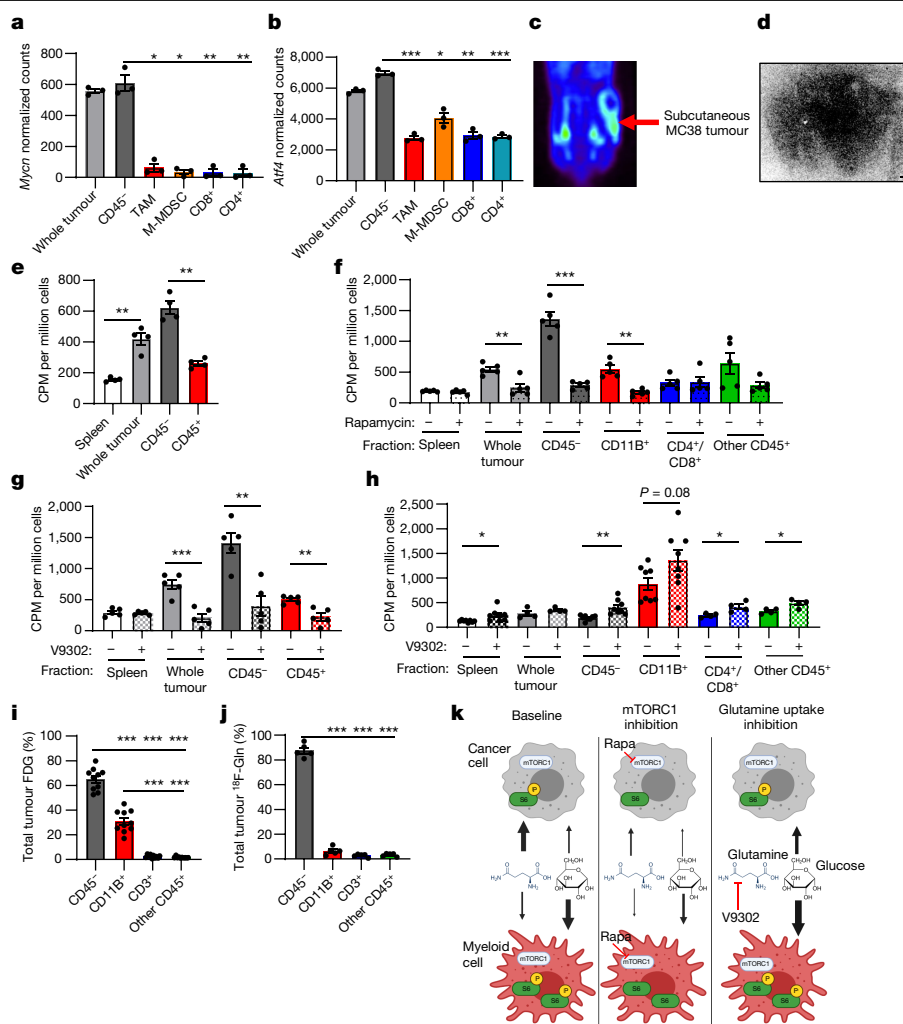
Fig. 4 | Glutamine partitions into cancer cells in the TME. a, b, mRNA transcript levels of glutamine-related transcription factors *Mycn* (**a**) and *Atf4* (**b**) in flow-sorted MC38 tumour cell populations (*n* = 3 mice). **c**, Representative ^{18}F-Gln PET image of a subcutaneous MC38 tumour. **d**, ^{18}F-Gln autoradiography image of a subcutaneous MC38 tumour. Scale bar, 800 μm. **e**, Cellular ^{18}F-Gln avidity in designated MC38 tumour cell fractions (*n* = 4 mice). **f, g**, Cellular ^{18}F-Gln avidity in MC38 tumour cell fractions from mice treated with vehicle or rapamycin (**f**) or with vehicle or V9302 (**g**) (*n* = 5 mice per group). **h**, FDG avidity in MC38 tumour cell fractions from mice treated with V9302 or dimethyl sulfoxide (DMSO) (*n* = 4 mice for whole tumour, CD4^{+}/CD8^{+} and other CD45^{+};

n = 8 mice for all others). **i, j**, Contribution of cell populations to total MC38 tumour FDG (**i**) (*n* = 10 mice) and ^{18}F-Gln signal (*n* = 5 mice) (**j**). **k**, Model for nutrient partitioning in the TME. Each data point represents a biological replicate; data are mean ± s.e.m. Data are representative of at least two independent experiments; **h** represents the combined data of two independent experiments. *P* values were calculated using Welch's two-tailed *t*-test (**e**–**h**) or the Brown–Forsythe and Welch ANOVA with Dunnett's T3 for multiple comparison tests (**a, b, i, j**); *P < 0.05, **P < 0.01, ***P < 0.001; exact *P* values are provided in the Source Data.

acidification rate (ECAR) and mitochondrial oxygen consumption rate (OCR) than tumour-infiltrating T cells and cancer cells (Fig. 2i–k). These studies show that TAMs and M-MDSCs consume the most glucose per cell in the TME and maintain robust glucose metabolism. Consistently with this, myeloid infiltration has been correlated with FDG avidity in non-tumour-bearing lymph nodes in human and mouse gynaecological malignancies[18]. Our data extend these findings directly to the TME and reveal the relative metabolic phenotypes of heterogeneous cells in the TME.

mTORC1 programs metabolism in the TME

Mammalian target of rapamycin complex 1 (mTORC1) supports anabolic metabolism and nutrient uptake[19]. We observed mTORC1 pathway activity by higher levels of phosphorylated ribosomal protein S6 (pS6) in tumour myeloid cells compared to other subsets of tumour cells in human clear cell renal cell carcinoma (ccRCC) and in mouse MC38 and

CT26 tumours (Fig. 3a–c, Extended Data Fig. 7a, Supplementary Table 1, Supplementary Fig. 1). To determine whether mTORC1 supports glucose uptake in the TME, we treated mice bearing MC38 tumours with rapamycin for four days and measured FDG uptake in tumour cell populations. Rapamycin did not affect tumour weight or concentrations of glucose, glutamine or lactate in the TME, but led to significant decreases in pS6 levels, T cell infiltration, Ki67 levels in cancer cells and T cells, and the cell size of TAMs (Fig. 3d, Extended Data Fig. 7b–f). Treatment with rapamycin also resulted in significant decreases in FDG uptake in myeloid and cancer cells (Fig. 3e). Extracellular flux demonstrated that in vivo treatment with rapamycin led to a decrease in myeloid cell metabolism ex vivo, whereas cancer cells and T cells remained unchanged (Fig. 3f–h). Tumour CD8^{+} T cells and TAMs retained phenotypic markers after treatment with rapamycin, but CD8^{+} T cells exhibited a functionally less activated phenotype (Extended Data Fig. 7g–n, Supplementary Fig. 1).

Flow-sorted CD45^{−} cancer cells, TAMs, M-MDSCs, CD8^{+} T cells and CD4^{+} T cells from MC38 tumours were transcriptionally profiled (Extended

Data Fig. 8a). In untreated tumours, principal component analysis and unbiased clustering based only on metabolism-related transcripts grouped samples by cell identity (Fig. 3i, Extended Data Fig. 8b, Supplementary Table 2). Corresponding with the increased uptake of glucose in myeloid cells, gene set enrichment analysis revealed a relative enrichment of glucose-related pathways in M-MDSCs and TAMs (Extended Data Fig. 8c, Supplementary Table 3). Genes encoding glucose transporters showed population-specific expression, with cancer cells and myeloid cells expressing high transcript levels of *Slc2a1* (GLUT1) and T cells expressing high levels of *Slc2a3* (GLUT3). *Hk2* and *Hk3*—encoding hexokinase isoforms 2 and 3, which catalyse glucose phosphorylation in cells as the rate-limiting first phosphorylation step of glucose in glycolysis—were most highly expressed in myeloid cells, in contrast to *Hk1*, which was broadly expressed. CD45^{−} cancer cells were enriched in transcripts relating to amino acids, lipids and signalling, and CD8^{+} T cells were enriched in nucleotide-related transcripts. Rapamycin increased the levels of glycolysis-related transcripts, particularly in CD45^{−} cancer cells, whereas the transcripts of other metabolic genes decreased, including amino-acid-related transcripts (Extended Data Fig. 9a–e, Supplementary Table 4). Levels of gene expression and changes after rapamycin treatment were confirmed at the protein level by flow cytometry. Treatment with rapamycin reduced the levels of HK1 across tumour cell populations and reduced the levels of HK2 specifically in TAMs, potentially underlying the differences between tumour cell types in glucose uptake (Fig. 3j, k). GLUT1 levels remained unchanged after rapamycin treatment (Extended Data Fig. 9f), but the protein levels of the iron transporter CD71 and the amino acid transporter CD98 decreased (Fig. 3l, m).

Cancer cells take up glutamine and lipids

Having shown that systemic glucose is preferentially consumed by tumour-infiltrating myeloid cells, we hypothesized that other nutrients also have distinct patterns of uptake in the TME. Ex vivo uptake of fluorescently labelled palmitate (C16 BODIPY) was highest in CD45^{−} cancer cells, corroborating our transcript enrichment data and showing that other nutrients may partition in a different manner to glucose in the TME (Extended Data Fig. 10a–c). On the basis of transcript data, we postulated that glutamine uptake would also be greatest in CD45^{−} cancer cells. Glutamine metabolism in the TME has been shown to promote cancer cell growth while impairing anti-tumour immunity[9]. MYCN and ATF4 drive the consumption of glutamine by cells[20], and *Mycn* and *Atf4* were more highly expressed in MC38 cancer cells than in immune cells (Fig. 4a, b). *Aspa*, *Asns* and *Gls2*, which encode enzymes that are involved in glutamine metabolism, were also specifically expressed in the MC38 cancer cells, as were the amino-acid-related transcripts *Pycr1* and *Slc7a5* (Extended Data Fig. 8b). Tumour-bearing mice were injected with ¹⁸F-(2*S*,4*R*)4-fluoroglutamine (¹⁸F-Gln) to measure glutamine pool size and uptake in the TME[21]. Subcutaneous MC38 tumours exhibited a high ¹⁸F-Gln avidity (Fig. 4c, d). In contrast to FDG, however, CD45^{−} cancer cells showed a greater avidity for ¹⁸F-Gln than did CD45^{+} immune cells in MC38 (Fig. 4e), CT26, Renca and spontaneous AOM/DSS tumour models (Extended Data Fig. 10d–f).

Treatment with rapamycin reduced amino-acid-related transcripts and CD98 protein levels in MC38 tumour cells. Correspondingly, rapamycin treatment sharply decreased the uptake of ¹⁸F-Gln in CD45^{−} and myeloid cells (Fig. 4f). To assess the relationship between glutamine and glucose uptake, tumour-bearing mice were treated with V9302—a small-molecule inhibitor of glutamine transport[22]. Treatment with V9302 broadly decreased the uptake of glutamine in cells in the TME (Fig. 4g), but increased the uptake of glucose in all tumour cell populations in the TME (Fig. 4h). V9302 also decreased MC38 tumour mass and T cell infiltration (Extended Data Fig. 10g, h) and increased the frequency of tumour M2-like macrophages (Extended Data Fig. 10i, j). Together, these data show that glutamine uptake and metabolism actively restrain glucose metabolism in vivo and that tumour-infiltrating

cells can access and increase glucose uptake beyond basal levels when glutamine is restricted. Cell-intrinsic programs of distinct tumour cell subsets thus dictate glucose and glutamine uptake in the TME.

Selective nutrient partitioning

Our findings show that discrete metabolic selections regulate glucose and glutamine uptake within the TME. In the context of the whole tumour, multiplying the per-cell glucose uptake by the abundance of each cell type revealed that cancer cells accounted overall for approximately two-thirds of glucose uptake, with myeloid cells accounting for another third and other immune cells having a negligible contribution (Fig. 4i). By contrast, the uptake of glutamine and lipids, both per cell and in the total tumour, was dominated by cancer cells (Fig. 4j, Extended Data Fig. 10c). These results support the notion that glucose is not grossly limiting in the TME and its use is instead modulated by cell-intrinsic programs and glutamine uptake (Fig. 4k).

Our work reveals that diverse cell populations preferentially acquire distinct metabolites from a common pool of metabolites available in the TME[11,23]. Tumour myeloid cells consume markedly more glucose than do tumour-infiltrating T cells or cancer cells on a per-cell basis, and tumour-infiltrating immune cells are more active than those in the spleen. This has implications for metabolism-directed agents as well as therapies that target myeloid cells, with the potential to either enhance or impair tumour-related inflammation. Our data also suggest that targeting glutamine metabolism could be used as a specific strategy to hamper the growth of cancer cells while also increasing glucose consumption and altering immunophenotype in the TME.

Previous studies have suggested that competition for glucose in the TME between cancer cells and T cells contributes to immunosuppression[3,4,24]. Our data, however, show that glucose is not broadly limiting, and that TME-resident cells have the capacity to increase glucose uptake in vivo when glutamine uptake is restricted. This cell-intrinsic programming provides a new level of insight into the inner workings of the TME. In this setting, a program of mTORC1-driven uptake of glutamine may suppress the expression of glycolysis-related genes and glucose metabolism in cancer cells. There is also growing evidence that glycolytic transcriptional programs in cancer cells are associated with immunosuppressive TMEs and directly recruit suppressive myeloid cells[25,26], whereas glycolysis in TAMs may drive hypoxia through endothelial dysfunction[27] and cytokine production[28]. Our work supports a model in which glycolytic tumours are immunoinhibitory not directly due to nutrient deficiencies but rather because of large-scale microenvironmental changes that alter intrinsic cellular programming, and in which different nutrients may follow distinct but cell- and tumour-type-specific patterns.

Myeloid cells directly consume FDG out of proportion to cancer cells and thus account for a considerable fraction (30%) of measured tumour glucose uptake in PET imaging. These findings also help to explain the intratumoral regional variability in FDG avidity that is observed on PET imaging, as well as the FDG-avid nature of Hodgkin's lymphoma, a disease in which far more inflammatory cells than transformed tumour cells are present. Understanding the biology of distinct cell types in the complex TME has contributed substantially to shaping models of tumorigenesis. Our studies extend these approaches to evaluate in vivo metabolic features of tumour cell types, and show that individual cell populations have distinct programs of nutrient uptake that may have an important role in their response or resistance to cancer therapies.

Online content

Any methods, additional references, Nature Research reporting summaries, source data, extended data, supplementary information, acknowledgements, peer review information; details of author contributions and competing interests; and statements of data and code availability are available at https://doi.org/10.1038/s41586-021-03442-1.

1. Vander Heiden, M. G. & DeBerardinis, R. J. Understanding the intersections between metabolism and cancer biology. *Cell* **168**, 657–669 (2017).
2. Siska, P. J. et al. Mitochondrial dysregulation and glycolytic insufficiency functionally impair CD8 T cells infiltrating human renal cell carcinoma. *JCI Insight* **2**, e93411 (2017).
3. Ho, P. C. et al. Phosphoenolpyruvate is a metabolic checkpoint of anti-tumor T cell responses. *Cell* **162**, 1217–1228 (2015).
4. Chang, C. H. et al. Metabolic competition in the tumor microenvironment is a driver of cancer progression. *Cell* **162**, 1229–1241 (2015).
5. Faubert, B. et al. Lactate metabolism in human lung tumors. *Cell* **171**, 358–371 (2017).
6. Ma, E. H. et al. Metabolic profiling using stable isotope tracing reveals distinct patterns of glucose utilization by physiologically activated CD8^{+} T cells. *Immunity* **51**, 856–870 (2019).
7. Liu, P. S. et al. α-Ketoglutarate orchestrates macrophage activation through metabolic and epigenetic reprogramming. *Nat. Immunol.* **18**, 985–994 (2017).
8. Johnson, M. O. et al. Distinct regulation of Th17 and Th1 cell differentiation by glutaminase-dependent metabolism. *Cell* **175**, 1780–1795 (2018).
9. Leone, R. D. et al. Glutamine blockade induces divergent metabolic programs to overcome tumor immune evasion. *Science* **366**, 1013–1021 (2019).
10. Scharping, N. E. et al. Mitochondrial stress induced by continuous stimulation under hypoxia rapidly drives T cell exhaustion. *Nat. Immunol.* **22**, 205–215 (2021).
11. Sullivan, M. R. et al. Quantification of microenvironmental metabolites in murine cancers reveals determinants of tumor nutrient availability. *eLife* **8**, e44235 (2019).
12. Cortese, N. et al. Metabolome of pancreatic juice delineates distinct clinical profiles of pancreatic cancer and reveals a link between glucose metabolism and PD-1^{+} cells. *Cancer Immunol. Res.* **8**, 493–505 (2020).
13. Gemta, L. F. et al. Impaired enolase 1 glycolytic activity restrains effector functions of tumor-infiltrating CD8^{+} T cells. *Sci. Immunol.* **4**, eaap9520 (2019).
14. Sinclair, L. V., Barthelemy, C. & Cantrell, D. A. Single cell glucose uptake assays: a cautionary tale. *Immunometabolism* **2**, e200029 (2020).
15. Nair-Gill, E. et al. PET probes for distinct metabolic pathways have different cell specificities during immune responses in mice. *J. Clin. Invest.* **120**, 2005–2015 (2010).
16. Hesketh, R. L. et al. Magnetic resonance imaging is more sensitive than PET for detecting treatment-induced cell death-dependent changes in glycolysis. *Cancer Res.* **79**, 3557–3569 (2019).
17. Spranger, S., Dai, D., Horton, B. & Gajewski, T. F. Tumor-residing Batf3 dendritic cells are required for effector T cell trafficking and adoptive T cell therapy. *Cancer Cell* **31**, 711–723 (2017).
18. Mabuchi, S. et al. Pretreatment tumor-related leukocytosis misleads positron emission tomography-computed tomography during lymph node staging in gynecological malignancies. *Nat. Commun.* **11**, 1364 (2020).
19. Saxton, R. A. & Sabatini, D. M. mTOR signaling in growth, metabolism, and disease. *Cell* **168**, 960–976 (2017).
20. Yoshida, G. J. Beyond the Warburg effect: N-Myc contributes to metabolic reprogramming in cancer cells. *Front. Oncol.* **10**, 791 (2020).
21. Zhou, R. et al. [^{18}F](2*S*,4*R*)4-Fluoroglutamine PET detects glutamine pool size changes in triple-negative breast cancer in response to glutaminase inhibition. *Cancer Res.* **77**, 1476–1484 (2017).
22. Schulte, M. L. et al. Pharmacological blockade of ASCT2-dependent glutamine transport leads to antitumor efficacy in preclinical models. *Nat. Med.* **24**, 194–202 (2018).
23. Kilgour, M. K. et al. 1-Methylnicotinamide is an immune regulatory metabolite in human ovarian cancer. *Sci. Adv.* **7**, eabe1174 (2021).
24. Cascone, T. et al. Increased tumor glycolysis characterizes immune resistance to adoptive t cell therapy. *Cell Metab.* **27**, 977–987 (2018).
25. Li, W. et al. Aerobic glycolysis controls myeloid-derived suppressor cells and tumor immunity via a specific CEBPB isoform in triple-negative breast cancer. *Cell Metab.* **28**, 87–103 (2018).
26. Chafe, S. C. et al. Targeting hypoxia-induced carbonic anhydrase IX enhances immune-checkpoint blockade locally and systemically. *Cancer Immunol. Res.* **7**, 1064–1078 (2019).
27. Wenes, M. et al. Macrophage metabolism controls tumor blood vessel morphogenesis and metastasis. *Cell Metab.* **24**, 701–715 (2016).
28. Jeong, H. et al. Tumor-associated macrophages enhance tumor hypoxia and aerobic glycolysis. *Cancer Res.* **79**, 795–806 (2019).

Article

Methods

Patient samples

Fresh histology-confirmed ccRCC tumours and matched healthy tissue were surgically removed from 14 patients. Supplementary Table 1 contains relevant patient and tumour information. Tumours and matched healthy kidney tissue were processed by mechanical dissociation (human tumour setting two on a Miltenyi gentleMACS) in Hanks' balanced salt solution (HBSS) with calcium chloride and magnesium chloride. Mechanical dissociation was followed by enzymatic digestion in 435 U ml^{-1} DNase I (Sigma-Aldrich, D5025) and 218 U ml^{-1} collagenase (Sigma-Aldrich, C2674) in RPMI supplemented with 10% FBS, 1% glutamine, 1% penicillin–streptomycin, 1% HEPES and 0.1% 2-mercaptoethanol for 30–45 min, depending on tissue toughness, at room temperature with agitation at 17 rpm. Tissue digests were washed with HBSS without calcium chloride, magnesium chloride or magnesium sulfate and then incubated in 5 mM EDTA for 20 min at room temperature with agitation at 17 rpm. Tumour and matched healthy kidney digests were washed with HBSS with calcium chloride and magnesium chloride. Then they were passed through a 70-µm filter and ACK-lysed. Patient PBMCs were isolated by density gradient centrifugation using Ficoll-Paque (GE Healthcare, 17144002) in SepMate-50 tubes (StemCell Technologies, 85450) and subsequently ACK-lysed. Single-cell suspensions were frozen in 90% FBS, 10% DMSO. Batched tumour and matched PBMCs were thawed, rested for 10 min at 37 °C, counted, stained and analysed for flow cytometry. All studies were conducted in accordance with the Declaration of Helsinki principles under a protocol approved by the Vanderbilt University Medical Center (VUMC) Institutional Review Board (protocol no. 151549). Informed consent was received from all patients before inclusion in the study by the Cooperative Human Tissue Network at VUMC.

Interstitial fluid collection and LC–MS metabolite analysis

Tissue interstitial fluid was collected from freshly resected ccRCC tumours and matched healthy kidney tissue. Specimens were centrifuged against a 0.22-µm nylon filter (Corning CLS8169) at 4 °C for 5 min at 300g. Flow-through tissue interstitial fluid was flash-frozen and stored at −80 °C before batch analysis. Mouse blood was collected through the submandibular vein, aliquoted immediately into EDTA and centrifuged for 10 min at 850g at 4 °C. Plasma supernatant was collected and then cleared by centrifugation for 20 min at 3,000g at 4 °C. Liquid chromatography–mass spectrometry (LC–MS) quantification of metabolites was performed as described previously[11].

Mice

C57BL/6J (000664), BALB/cJ (000651), $Rag1^{-/-}$ (002216) and OTI transgenic (003831) mice were obtained from The Jackson Laboratory. All mouse procedures were performed under Institutional Animal Care and Use Committee (IACUC)-approved protocols from VUMC and conformed to all relevant regulatory standards. Mice were housed in ventilated cages with at most five mice per cage and were provided with ad libitum food and water. Mice were on 12-h light–dark cycles which coincided with daylight in Nashville, TN. The mouse housing facility was maintained at 20–25 °C and 30–70% humidity. For injectable tumour models, 8–20-week old male and female mice were used. Mice were euthanized if the humane end-point was reached (tumours of 2-cm dimension, ulceration, weight loss of more than 10%). V9302 treatments were administered intraperitoneally twice daily for 5 days at 25 mg kg^{-1} for FDG uptake or once at 75 mg kg^{-1} 3 h before ^{18}F-Gln injection. Rapamycin treatments were administered intraperitoneally daily for 4 days at 2 mg kg^{-1} dissolved in 2% DMSO, 30% polyethylene glycol 300 (Sigma-Aldrich, 202371) and 5% Tween 80 (Sigma-Aldrich, P1754). Mice were randomized at the first day of treatment to control or drug in an unblinded manner, with mice from the same cage receiving different treatments. Sample sizes were chosen based on prior experiments.

Cell lines

The MC38 and CT26 cell lines were provided by B. Fingleton and grown in DMEM supplemented with 10% FBS. The Renca cell line was obtained through ATCC and grown in RPMI 1640 supplemented with 10% FBS, 4 mM glutamine, 25 mM HEPES, essential amino acids and sodium pyruvate. Cells were trypsinized and washed twice in PBS, and 1×10^6 cells were injected subcutaneously in 100–200 µl PBS on mouse flanks. Subcutaneous tumours grew for 14 days before analysis. The MC38-EL-THY1.1 cells were generated using a transposon-based engineering approach with plasmids that were described previously[29]. MC38 cells were electroporated using the Neon transfection system (Thermo Fisher Scientific) according to the manufacturer's recommendations for adherent cell lines. A total of 5 million MC38 cells were suspended in electroporation buffer containing 5 µg of the plasmid pCMV-M7PB and 15 µg of the plasmid pT-EL-THY1.1, which is a bicistronic transposon vector driving expression of an enhanced firefly luciferase as well as THY1.1 antigen. Cells were magnetically sorted on the basis of their expression of THY1.1 using magnetic beads (Miltenyi, 130-121-273). Cell lines were regularly tested for mycoplasma using PCR and all cells used in downstream assays were confirmed negative.

Orthotopic renal implantation

For intrarenal Renca injections, survival mouse surgery was performed according to a previously described method[30]. In brief, mice were anesthetized by isoflurane inhalation at 2–3% and placed on a warming recirculating water pad set at 37 °C to maintain body temperature. Using sterile surgical techniques, a 1-cm incision was made in the skin running parallel to the spine, slightly below the ribcage on the right flank. Next, a 1-cm incision was made in the muscle layer in the same location. Using gentle pressure on the mouse abdomen, the right kidney was exteriorized. A total of 5×10^4 Renca cells resuspended in 100 µl PBS were injected using a 29-gauge needle inserted through the renal capsule into the cortical space. The injection site was swabbed using sterile gauze and the kidney was returned to the body cavity. The abdominal wall was closed using 6-0 monofilament absorbable sutures (AD Surgical, S-D618R13), and the skin was closed using wound clips. Analgesia was provided pre-surgery and 24 h after surgery in the form of ketoprofen injections at 5 mg kg^{-1}. Wound clips were removed seven days after the surgery. Tumours were analysed 28 days after cancer cell injection.

Spontaneous tumour models

PyMT GEMM mice were bred by crossing male transgenic mice expressing the PyMT oncoprotein under the MMTV-LTR promoter (Jackson Laboratory, 022974) with wild-type females on a similar B6/FVB mixed background. The GEMM mice were from a colony in which all mice expressed two *Vhl* alleles in which exon 1 is flanked by *loxP* sites (Jackson Laboratory, 012933) but did not express a *cre* transgene and were thus effectively wild type. Once weaned, female mice were palpated twice a week and tumours were measured in three dimensions with digital calipers. Mice were collected when any tumour had grown to a size of 1 cm in diameter in any dimension, around 5 months of age. Virgin female littermates were used in these studies.

The AOM/DSS inflammatory CRC model was used as previously described[31,32]. In brief, bedding was mixed to normalize the microbiome two weeks before experimental initiation. Eight-to-twelve-week-old C57BL/6J mice were intraperitoneally injected with 12.5 mg kg^{-1} AOM and exposed to three 4-day cycles of 3% to 4% DSS (TdB Labs, 9011-18-1). Each DSS cycle was followed by a 16-day recovery period. Before euthanasia, colonoscopy was performed to confirm tumour development. Mice were weighed every other day throughout the experiment. Mice were euthanized 6–8 weeks after completing the last cycle of DSS. Colons were dissected and tumour tissue was isolated from the mucosa.

PET–CT imaging

For individual studies, a group of MC38-tumour-bearing mice were food-restricted overnight. Then the mice received a retro-orbital injection of around 37 MBq/0.1 ml of ^{18}F-FDG and were returned to plate-warmed cages. Forty minutes later, the mice were anaesthetized under 2% isofluorane and imaged using an Inveon microPET (Siemens Preclinical) for 20 min. Data from all possible lines of response were saved in the list mode raw data format. The raw data were then binned into 3D sinograms with a span of 3 and ring difference of 47. The images were reconstructed into transaxial slices ($128 \times 128 \times 159$) with voxel sizes of $0.0815 \times 0.0815 \times 0.0796 \, cm^3$, using the MAP algorithm with 16 subsets, 4 iterations and a beta of 0.0468. For anatomical co-registration, immediately following the PET scans, the mice received a computer tomography (CT) scan in a NanoSPECT/CT (Mediso) at an X-ray beam intensity of 90 mAs and an X-ray peak voltage of 45 kVp. The CT images were reconstructed into $170 \times 170 \times 186$ voxels at a voxel size of $0.4 \times 0.4 \times 0.4 \, mm^3$. The PET–CT images were uploaded to Amide (www.sourceforge.com) and volumetric regions of interest (ROIs) were drawn around the tumours. The PET images were normalized to the injected dose and the mean radiotracer concentration within the ROIs were determined.

^{18}F autoradiography

Mice were handled and injected in a similar manner to that described for the PET–CT imaging, but without overnight fasting. Tumours were collected, embedded in optimal cutting temperature compound (OCT, Thermo Fisher Scientific, 23-730-571) and frozen on dry ice. Tumours were cut into 10-μm sections and imaged in a Beta Imager (Biospacelabs) for 1 h. ROIs were drawn around the resulting tumour and spleen images and the counts in each ROI were compared.

^{18}F-FDG and ^{18}F-Gln nutrient uptake assay

Tumour-bearing mice were retro-orbitally injected with 1 mCi of FDG or ^{18}F-Gln synthesized at VUMC[33]. During radiotracer uptake, mice were conscious and had access to food and water. Mice were euthanized and spleen and tumours were collected 40 min after radiotracer administration. Single-cell suspensions of splenocytes were prepared by physical dissociation followed by ACK-lysis. Tumours were chopped, mechanically dissociated on the Miltenyi gentleMACS Octo Dissociator with Heaters (setting implant tumour one) and digested in 435 U ml^{-1} DNase I (Sigma-Aldrich, D5025) and 218U ml^{-1} collagenase (Sigma-Aldrich, C2674) at 37 °C for 30 min. After enzyme treatment, tumours were passed through a 70-μm filter and ACK-lysed. Cells were resuspended in MACS buffer (PBS + 2% FBS + 2 mM EDTA) and counted using trypan blue with the TC20 Automated Cell Counter (Bio-Rad). In some cases, tumours from different mice were pooled to achieve a higher number of tumour cells before fractionation to ensure sufficient ^{18}F signal, and were ultimately analysed as biological replicates. Next, tumour cell suspensions were fractionated using serial magnetic bead positive selection according to the manufacturer's instructions (all Miltenyi mouse kits: CD45 TIL 130-110-618, EPCAM 130-105-958, THY1.1 130-121-273, CD4/CD8 TIL 130-116-480, CD11B 130-049-601, F4/80 130-110-443, GR1 130-094-538, CD11C 130-125-835). In brief, cells were resuspended at 10 million total cells per 90 μl MACS buffer and 10 μl microbeads for 15 min. Then, cell suspensions were applied to LS columns (Miltenyi, 130-042-401) in Miltenyi QuadroMACS Separators, washed and eluted according to the manufacturer's instructions. Fractions were resuspended in 1 ml medium; 10 μl was used for trypan blue staining and TC20 cell count, around 50 μl was stained for flow cytometry determination of fraction cellular composition, and 900 μl was transferred into 5-ml tubes to measure radioactivity. Nine hundred microlitres of 2-ml splenocyte suspensions and 5 million total cells from the unfractionated whole tumour were also assayed for radioactivity. The Hidex Automatic Gamma Counter was used with 1-min read times

to measure time-normalized ^{18}F CPM for each sample. To determine per cell ^{18}F-nutrient avidity, time-normalized CPM was divided by the number of viable cells as determined by trypan count. Collected tissues and cell fractions were kept on ice or at 4 °C in RPMI 1640 supplemented with 10% FBS except when noted.

Flow cytometry

Single-cell suspensions obtained from tumours and spleens were incubated in F_c block (1:50, BD, 553142) for 10 min at room temperature, stained for surface markers for 15 min at room temperature, washed with FACS buffer (PBS + 2% FBS) once and resuspended in FACS buffer for analysis on a Miltenyi MACSQuant Analyzer 10 or 16. For intracellular staining, the eBioscience FOXP3/transcription factor staining buffer kit (Thermo Fisher Scientific, 00-5523-00) was used. For intracellular cytokine staining, tumour single-cell suspensions were incubated for 4 h at 37 °C, 5% CO_2 in supplemented RPMI with PMA (50 ng ml^{-1}, Sigma-Aldrich, P8139-1MG), ionomycin (750 ng ml^{-1}, Sigma-Aldrich, I0634-1MG) and GolgiPlug (1:1,000, BD, 555029), and processed using the BD Cytofix/Cytoperm Fixation and Permeabilization Solution (Thermo Fisher Scientific, BDB554722). Surface staining was performed as described above, cells were fix/permed for 20 min at 4 °C, and then stained for intracellular markers for at least 30 min at 4 °C. Ghost Dye Red 780 viability dye (1:4,000, Cell Signaling, 18452S) was used identically to surface antibodies. The anti-mouse and cross-reactive antibodies used were: CD45 BV510 (1:1,600, 30-F11, Biolegend, 103138), B220 e450 (1:400, RA3-6B2, Thermo Fisher Scientific, 48-0452-82), CD11B e450 (1:1,600, M1/70, Thermo Fisher Scientific, 48-0112-82), CD11B FITC (1:1,600, M1/70, Biolegend, 101206), CD8A AF488 (1:1,600, 53-6.7, Biolegend, 100723), CD8A BV510 (1:600, 53-6.7, BD, 563068), LY6C FITC (1:4,000, HK1.4, Biolegend, 128006), CD11C PE (1:1,000, N418, BioLegend, 117308), FOXP3 PE (1:125, FJK-16 s, Thermo Fisher Scientific, 12-5773-82), pS6 Ser235/236 PE (1:100, D57.2.2E, Cell Signaling, 5316S), CD4 PerCP-Cy5.5 (1:600, RM4-5, BioLegend, 100540), LY6G PerCP-Cy5.5 (1:800, 1A8, BioLegend, 127616), F4/80 PE-Cy7 (1:800, BM8, BioLegend, 123114), NKp46 PE-Cy7 (1:200, 29A1.4, BioLegend, 137618), CD3 PE-Cy7 (1:200, 17A2, BioLegend, 100220), CD3 FITC (1:200, 17A2, BioLegend, 100204), CD3 APC (1:200 17A2, BioLegend, 100236), CD206 APC (1:500, C068C2, BioLegend, 141708), GLUT1 AF647 (1:500, EPR3915, Abcam, ab195020), EPCAM PE (1:1500, G8.8, BioLegend, 118206), THY1.1 PerCP-Cy5.5 (1:2,000, HIS51, Thermo Fisher Scientific, 45-0900-82), CD45 PE (1:1,600, 30-F11, Thermo Fisher Scientific, 12-0451-83), LY6C BV570 (1:400, HK1.4, BioLegend, 128030), CD68 BV605 (1:200, FA-11, BioLegend, 137021), HK1 AF647 (1:100, EPR10134(B), Abcam, ab197864), HK2 AF647 (1:200, EPR20839, Abcam, EPR20839), CD71 APC (1:100, RI7217, BioLegend, 113820), CD98 PE (1:400, RL388, Thermo Fisher Scientific, 12-0981-81), MHCII I-A/I-E APC (1:4,000, M5/114.15.2, BioLegend, 107614), CD103 PE-Cy7 (1:200, 2E7, BioLegend, 121425), LAG3 e450 (1:100, eBioC9B7W, Thermo Fisher Scientific, 48-2231-82), PD1 PE (1:100, 29F-1A12, BioLegend, 135206), TIM3 APC (1:100, RMT3-23, BioLegend, 119706), IFNγ APC (1:250, XMG1.2, BioLegend, 505810), CD25 e450 (1:500, PD61.5, Thermo Fisher Scientific, 48-0251-82), CD44 PE-Cy7 (1:1,000, IM7, BioLegend, 103030) and CD62L APC (1:200, MEL-14, Thermo Fisher Scientific, 17-0621-82). The anti-human antibodies used were: CD45 BV421 (1:400, HI30, BioLegend, 304032), CD3 APC (1:200, UCHT1, BioLegend, 300439), CD11B PerCP-Cy5.5 (1:200, ICRF44, BioLegend, 301328), CD14 BV510 (1:200, M5E2, BioLegend, 301842), CA9 AF647 (1:200, 303123, R&D Systems, FAB2188R-100UG) and Human Fc Block (1:50, BD 564220). For in vivo intravenous CD45 PE labelling, MC38-tumour-bearing mice were injected with 5 μg anti-CD45 PE diluted to 150 μl in PBS via tail vein and euthanized 5 min later. For ex vivo fluorescent palmitate uptake, tumour single-cell suspensions were incubated for 1 h in Krebs buffer (125 mM NaCl, 2.5 mM KCl, 25 mM NaHCO$_3$, 1 mM NaH$_3$PO$_4$, 1 mM MgCl$_2$, 2.5 mM CaCl$_2$, pH 7.2) at 37 °C, 5% CO_2, incubated with BODIPY FL C16 (1μM in Krebs buffer, Thermo Fisher Scientific, D3821) for 45 min, washed twice with FACS and

Article

then stained for surface markers. For the myeloid suppression assay, microbead-isolated CD11B$^+$ myeloid cells were co-incubated with 100,000 CellTrace Violet (CTV)-labelled (Thermo Fisher Scientific, C34557) OT-I splenocytes per well in a 96-well plate in the presence of 1 µg ml^{-1} SIINFEKL peptide for 3 days before analysis by flow cytometry. Flow cytometry data were analysed using FlowJo v.10.7.1.

In vivo 2-NBDG and flow sorting

2-NBDG (Cayman Chemical 11046) was dissolved in PBS at 5 mM (1.71 mg ml^{-1}) and 100 µl (500 ng) was injected retro-orbitally. Mice were euthanized 40 min later and tumour cells and splenocytes were collected as indicated above. Splenic T cells were isolated according to the manufacturer's instructions using the Pan T Cell Isolation Kit (Miltenyi, 130-095-130). 2-NBDG$^{hi/lo}$ cells were collected on the Nanocellect WOLF cell sorter and subsequently gamma counted as described for the ^{18}F-FDG and ^{18}F-Gln nutrient uptake assay.

Immunohistochemistry and light microscopy

MC38 tumours were fixed overnight in 10% formalin and then switched to 70% ethanol. Single-colour IHC was performed by VUMC Translation Pathology Shared Resource. Staining was conducted on the Leica Bond Max IHC stainer. All steps besides dehydration, clearing and coverslipping were performed on the Bond Max. Slides were first deparaffinized. Antigen retrial and antibody dilution were altered for maximal staining with each antibody. For CD11B staining (Novus Biologicals, NB110-89474,) slides were placed in a Protein Block (DAKO, ref. x0909) for 10 min before staining. Then, the slides were incubated in epitope retrieval 2 solution for 10 min, and subsequently stained (1:10,000 dilution). For CD3 staining (Abcam, Ab16669), slides were incubated in epitope retrieval 2 solution for 10 min before staining (1:250 dilution). For F4/80 staining (Novus Biologicals, NB600-404LLC), epitope retrieval was conducted in proteinase K for 5 min before primary antibody staining (1:300 dilution). Rabbit anti-rat secondary (Vector Laboratories, BA-4001) was used at a 1:2,000 dilution for 15 min for antigen detection. For CD31 staining (Dianova, DIA-310), epitope retrieval occurred in epitope retrieval 2 solution for 20 min and slides were subsequently stained (1:75 µl dilution). Staining with biotinylated anti rat (Vector Laboratories, BA-4000) was used for antigen detection at a 1:2,000 dilution for 15 min. For CD45 staining (SySy Synaptic Systems, HS-427 017) epitope retrieval occurred in epitope retrieval solution 2 for 20 min, followed by primary antibody (1:500 dilution. Rabbit anti-rat secondary (Vector Laboratories, BA-4001) was used at a 1:2,000 dilution for 15 min to detect the antigen. The Bond Refine (DS9800) detection system was used for visualization. Images were captured using an Olympus BX53 microscope (Olympus Corporation), an Olympus DP73 camera and Olympus cellSens Standard imaging software v.1.17. Low-power images were captured with a 4× objective lens and high-power images were captured with a 40× objective lens.

MC38 anti-F4/80 microbead-fractionated TAMs were mounted onto slides using Wescor Cytopro cytocentrifuge and stained with H&E following yjr manufacturer's guidelines Thermo Fisher Scientific, 23-122952). Images were captured under oil immersion (100× objective) using an Olympus BX53 microscope (Olympus Corporation), an Olympus DP73 camera and Olympus cellSens Standard imaging software.

Extracellular flux assay

Tumour cell fractions were obtained as described above. Each fraction was plated at 200,000 live cells per well in technical quadruplicate on a Cell-Tak-coated plate (Corning 354240) in Agilent Seahorse RPMI 1640 supplemented with 10 mM glucose, 1 mM sodium pyruvate and 2 mM glutamine. Cells were analysed on a Seahorse XFe 96 bioanalyzer using the Mitostress assay (Agilent, 103015–100) with 1 µM oligomycin, 2 µM FCCP and 0.5 µM rotenone and antimycin A. Data were analysed in Agilent Wave software v.2.6.

Cell sorting and mRNA transcript analysis

CD45$^+$ and CD45$^-$ tumour cell fractions were obtained as described above. Cell fractions were stained for the indicated surface markers and viability dye and sorted on a BD FACSAria III cell sorter. RNA was isolated from tumour cell populations and unstained whole-tumour single-cell suspensions using the Quick-RNA Microprep Kit (Zymo R1050) according to the manufacturer's instructions. RNA transcripts were quantified using the NanoString nCounter Metabolic Pathways Gene Expression Panel (XT-CSO-MMP1-12) according to the manufacturer's instructions. Transcript counts of 768 genes enriched in cellular metabolic pathways were analysed using NACHO v1.0.1[34], an R package for parsing, visualization, quality control and normalization designed for NanoString nCounter data. While parsing raw transcript counts, manufacturer-designated housekeeping genes were used to normalize between samples: *Abcf1*, *Agk*, *Cog7*, *Dhx16*, *Dnajc14*, *Edc3*, *Fcf1*, *G6Pdx*, *Mrps5*, *Nrde2*, *Oaz1*, *Polr2a*, *Sap130*, *Sdha*, *Stk11ip*, *Tbc1d10b*, *Tbp*, *Tlk2*, *Ubb* and *Usp39*. Sample quality was evaluated based on normal ranges provided by the manufacturer for (1) binding density (0.1–2.25), (2) field of view (<75), (3) positive control linearity (<0.95) and (4) limit of detection (<2). Samples were excluded if they failed any of the four conditions. The third replicates of M-MDSC rapamycin and CD4$^+$ rapamycin were excluded as outliers for abnormal positive control linearity and limit of detection, respectively. Normalization was performed using geometric means based on housing genes, positive and negative controls. The normalized data from this experiment have been deposited in the Gene Expression Omnibus (GEO) and can be accessed at GSE165223. Principal component analysis was performed using the FactoMineRv2.3 package[35] in R. Differentially expressed metabolic genes were identified using a one-way ANOVA performed on transcript count across samples. *P* values were adjusted for multiple testing using Benjamini–Hochberg false discovery rate using the 'p.adjust' R function. For metabolic genes passing an adjusted *P* value of less than 0.01, we performed hierarchical clustering across samples and genes using default settings with the seaborn package (v. 0.11.0) in Python. On the basis of the hierarchical clustering, we grouped genes and performed gene set enrichment analyses using gProfiler[36] with Reactome gene sets compared to all genes. 'Metabolism' was the most highly enriched pathway for each cell type and was excluded from bar graphs for space. Differentially expressed genes between the rapamycin- and the vehicle-treated samples for each cell type were identified using edgeR[37] (v.3.28.1). First, the dispersion (variance of transcript counts) was estimated using the function 'estimateDisp'. Next, the differential expression between conditions was evaluated using a likelihood ratio test for a negative binomial generalized log-linear model. We considered transcripts with a false discovery rate of lower than 10% and/or a two-tailed *t*-test *P* value of less than 0.01 as being differentially expressed. All analyses were performed using R (v. 4.0.2).

Quantification and statistical analysis

Graphs and statistical tests were generated using GraphPad Prism v.9 unless otherwise noted. Sample sizes were chosen based on previous studies and no statistical methods were used to predetermine sample size. The experiments were not randomized and the investigators were not blinded to allocation during experiments and outcome assessment.

Reporting summary

Further information on research design is available in the Nature Research Reporting Summary linked to this paper.

Data availabilty

All data will be made available upon reasonable request to J.C.R. or W.K.R. Tumour mRNA transcript data that support the findings of this study have been deposited in the Gene Expression Omnibus (GEO)

with accession number GSE165223. These data are also found in Supplementary Table 4. Source data are provided with this paper.

Code availability

The code used to support tumour mRNA transcript analysis has been previously published (see Methods references) and will be made available upon request to J.C.R. or W.K.R.

29. O'Neil, R. T. et al. Transposon-modified antigen-specific T lymphocytes for sustained therapeutic protein delivery in vivo. *Nat. Commun.* **9**, 1325 (2018).
30. Tracz, A., Mastri, M., Lee, C. R., Pili, R. & Ebos, J. M. L. Modeling spontaneous metastatic renal cell carcinoma (mRCC) in mice following nephrectomy. *J. Vis. Exp.* **86**, 51485 (2014).
31. Parang, B., Barrett, C. W. & Williams, C. S. AOM/DSS model of colitis-associated cancer. *Methods Mol. Biol.* **1422**, 297–307 (2016).
32. Becker, C. et al. In vivo imaging of colitis and colon cancer development in mice using high resolution chromoendoscopy. *Gut* **54**, 950–954 (2005).
33. Hassanein, M. et al. Preclinical evaluation of 4-[^{18}F]Fluoroglutamine PET to Assess ASCT2 expression in lung cancer. *Mol. Imaging Biol.* **18**, 18–23 (2016).
34. Canouil, M. et al. NACHO: an R package for quality control of NanoString nCounter data. *Bioinformatics* **36**, 970–971 (2020).
35. Lê, S. Josse, J. Husson, & F. FactoMineR: A package for multivariate analysis. *J. Stat. Softw.* **25**, 1–18 (2008).
36. Raudvere, U. et al. g:Profiler: a web server for functional enrichment analysis and conversions of gene lists (2019 update). *Nucleic Acids Res.* **47**, W191–W198 (2019).
37. Robinson, M. D., McCarthy, D. J. & Smyth, G. K. edgeR: a Bioconductor package for differential expression analysis of digital gene expression data. *Bioinformatics* **26**, 139–140 (2010).

Extended Data Fig. 1 | Supporting data for Fig. 1. a–f, Fraction purity, viability and yield for MC38 (**a**; $n = 5$ mice), CT26 (**b**; $n = 4$ mice), and Renca (**c**; $n = 4$ mice) subcutaneous tumours; intrarenal Renca tumours (**d**; $n = 3$ mice); AOM/DSS CRC tumours (**e**; $n = 6$ mice for tumours, $n = 11$ mice for spleens); and spontaneous PyMT GEMM tumours (**f**; $n = 3$ mice). **g**, Representative flow cytometry analysis of PyMT and AOM/DSS CRC whole tumour, CD45+ immune cell and EPCAM+ cancer cell fractions gated on live cells. Each data point represents a biological replicate; data are mean ± s.e.m. Data are representative studies performed independently at least twice.
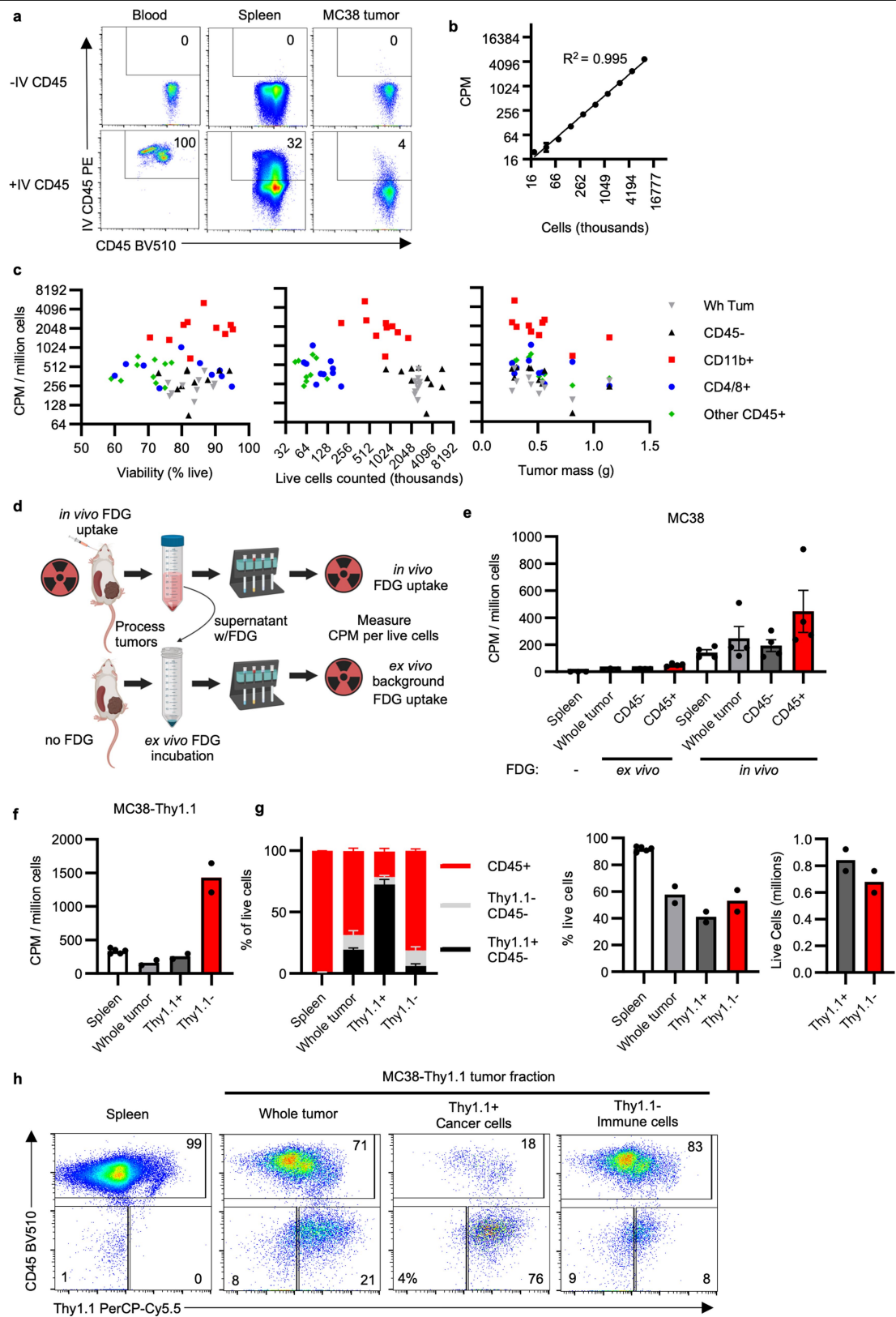
Extended Data Fig. 2 | See next page for caption.

Article

Extended Data Fig. 2 | Validation of in vivo cellular FDG uptake assay.
a, Intravenous (IV) anti-CD45 PE staining of leukocytes from designated tissues gated on live CD45$^+$ cells. **b**, Demonstration of dynamic range of ^{18}F quantification using serially diluted in vivo FDG-labelled splenocytes. **c**, Correlation plots of CPM per million live cells versus cell viability, cells counted and tumour mass across multiple tumour cell populations. Only the CD45$^-$ and other CD45$^+$ simple linear regressions had slopes significantly different than 0 for tumour mass (n = 10 mice). **d**, FDG-labelled digest supernatant from in vivo labelled MC38 tumours was applied to FDG-naive MC38 tumour single-cell suspensions to determine the contribution of ex vivo background FDG uptake to the final signal. **e**, Cellular FDG avidity in designated ex vivo and in vivo labelled MC38 tumour cell populations (n = 4 mice/group). **f**, Cellular FDG avidity in designated tumour cell fractions from MC38 THY1.1 tumours (n = 2 mice). **g**, Proportion of CD45$^+$ and THY1.1$^+$ cells, cell viability and live-cell yield from MC38 THY1.1 tumours (n = 2 mice for tumours; n = 5 mice for spleens). **h**, Representative flow cytometry analysis of MC38 THY1.1 tumour fractions. Each data point represents a biological replicate; data are mean ± s.e.m. Data in **b**, **d**–**h** are from a representative study performed independently at least twice.
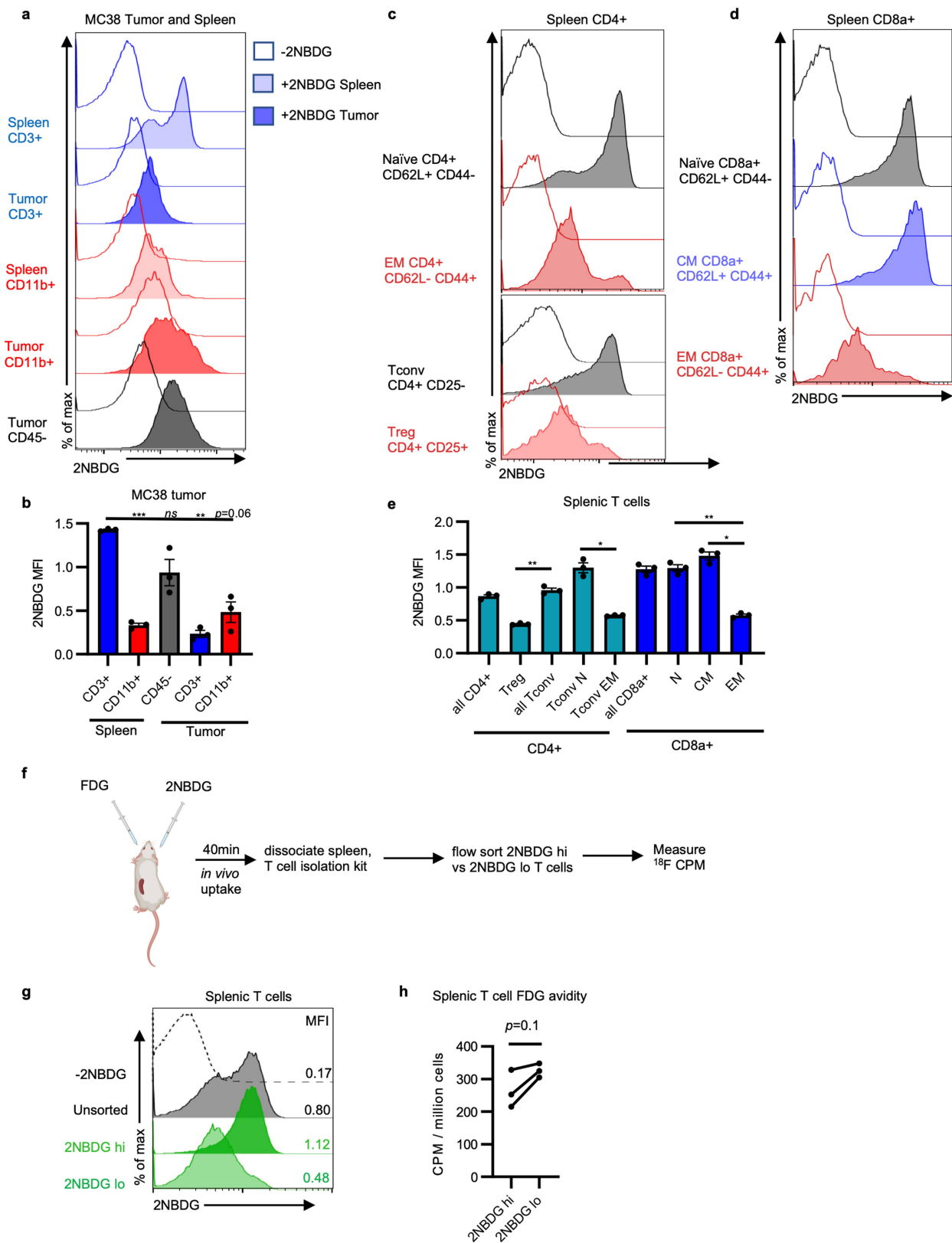
Extended Data Fig. 3 | See next page for caption.

Article

Extended Data Fig. 3 | In vivo 2-NBDG uptake does not mirror FDG uptake.
a, Representative histograms of in vivo 2-NBDG uptake in splenic and MC38 tumour cell subsets. **b**, MFI of in vivo 2-NBDG uptake across spleen and MC38 tumour cells ($n = 3$ mice). **c**, **d**, Representative histograms of 2-NBDG uptake in vivo in splenic CD4^{+} (**c**) and CD8^{+} (**d**) T cells. **e**, 2-NBDG staining in splenic CD4^{+} and CD8^{+} subsets ($n = 3$ mice). CM, central memory T cell; EM, effector memory T cell; N, naive T cell; T_{conv}, conventional CD4^{+} T cell; T_{reg}, regulatory CD4^{+} T cell. **f**, Schema for 2-NBDG and FDG co-injection experiment. **g**, Representative histogram of 2-NBDG^{hi} and 2-NBDG^{lo} populations collected through flow sorting. **h**, Per-cell FDG avidity of flow-sorted 2-NBDG[lo] versus 2-NBDG[ho] splenic T cells ($n = 3$ mice). Each data point represents a biological replicate; data are mean ± s.e.m. Data are from representative studies performed independently at least twice. P values were calculated using the Brown–Forsythe and Welch ANOVA with Dunnett's T3 for multiple comparison tests (**b**, **e**), two-tailed Welch's t-test for CD4^{+} comparisons (**e**) or a paired t-test (**h**); *$P < 0.05$, **$P < 0.01$, ***$P < 0.001$; exact P values are provided in the Source Data.
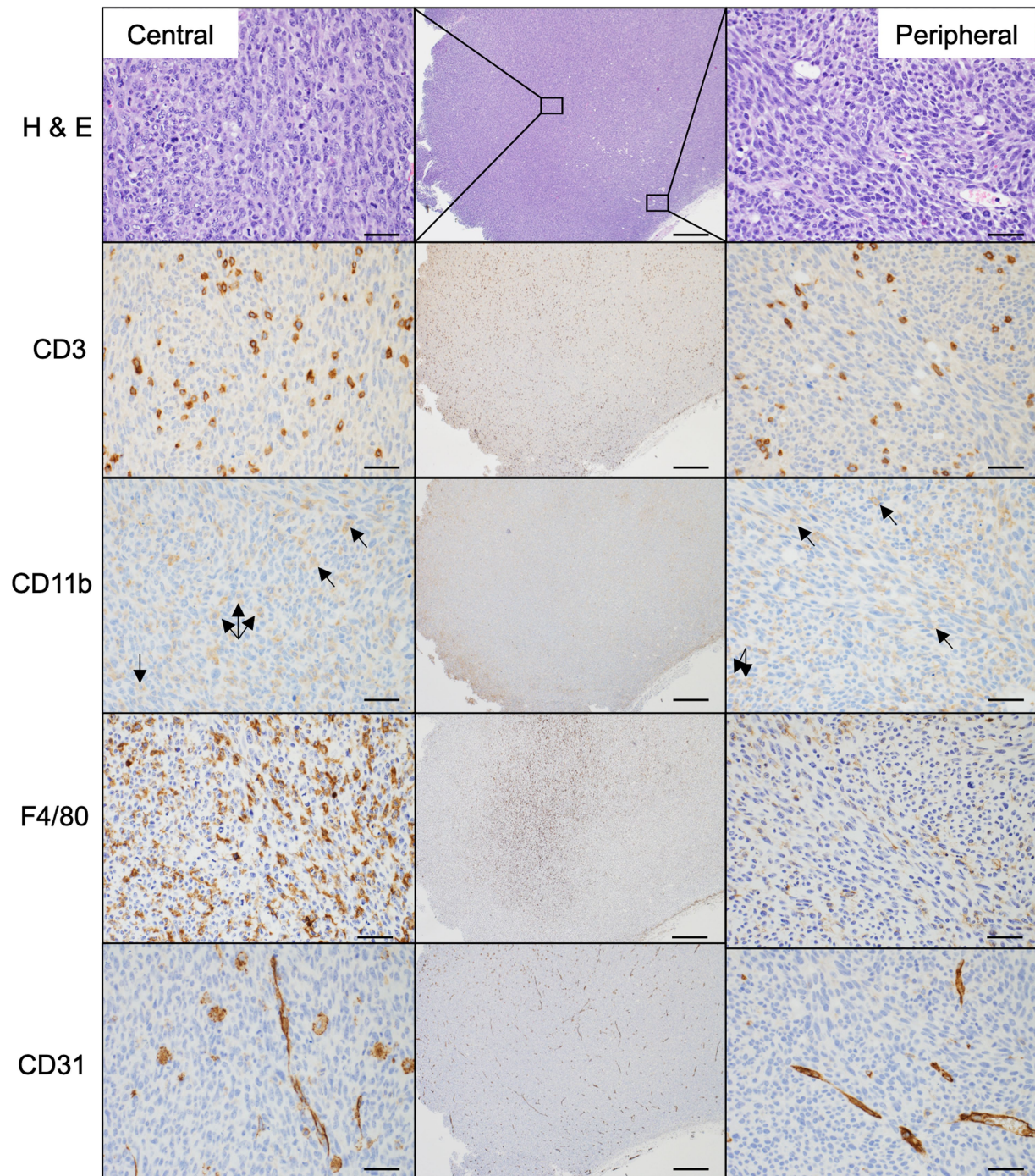
Extended Data Fig. 4 | Spatial organization of immune cells in subcutaneous MC38 tumours. Representative micrographs of H&E and indicated IHC stains of subcutaneous MC38 tumours. Arrows indicate positive cells on faint CD11B stain. The centre column is a low-power overview (scale bars, 200 μm). Insets demonstrate high-power images from central (left) and peripheral (right) tumour locations (scale bars, 20 μm). Images are representative of five biological replicates.

Extended Data Fig. 5 | Tumour model characterizations by flow cytometry.
a–**g**, Spleen and tumour CD45⁺ immune cell populations from MC38 (**a**; n = 3 mice), CT26 (**b**; n = 4 mice) and Renca (**c**; n = 4 mice) subcutaneous tumours; intrarenal Renca tumours (**d**; n = 3 mice); spontaneous PyMT GEMM tumours (**e**; n = 3 mice); AOM/DSS CRC tumours (**f**; n = 6 mice for tumours; n = 11 mice for spleens); and MC38 subcutaneous tumours grown in $Rag1^{-/-}$ mice (**g**; (n = 6

mice). DC, dendritic cell; NK cell: natural killer cell, PMN-MDSC, polymorphonuclear myeloid-derived suppressor cell. **h**, Gating strategy for immune cell identification using lymphocyte and myeloid-focused antibody panels. Each data point represents a biological replicate; data are mean ± s.e.m. Data in **a**–**f** are representative of independent experiments performed at least twice.

Extended Data Fig. 6 | See next page for caption.

Extended Data Fig. 6 | Supporting data for Fig. 2. a, **b**, Fraction composition, viability and live-cell yield from MC38 tumour fractions isolated using CD4⁺/CD8⁺ microbeads (n = 3 mice for tumours; n = 4 mice for spleens) (**a**) and CD11B⁺ microbeads (n = 4 mice) (**b**). **c**, **d**, Cellular FDG avidity in designated CT26 tumour cell fractions using CD4⁺/CD8⁺ microbeads (n = 5 mice for whole spleens; n = 3 mice for spleen fraction, other CD45⁺ and whole tumours; n = 4 mice for all others) (**c**) and CD11B⁺ microbeads (n = 5 mice for spleen fraction; n = 3 mice for whole tumours; n = 4 mice for all others) (**d**). **e**, **f**, Fraction composition, viability and live-cell yield from MC38 tumour fractions isolated using GR1⁺ microbeads (**e**) and F4/80⁺ microbeads (**f**) (n = 4 mice). **g**, Cellular FDG avidity in designated MC38 tumour cell fractions from *Rag1*⁻/⁻ mice (n = 6 mice). **h**, Cellular FDG avidity in MC38 tumour cell fractions using CD11B⁺ and CD11C⁺ microbeads (n = 9 mice for whole spleens; n = 5 mice for spleen fraction; n = 10 mice for all others). **i**, Fraction composition of CD11C⁺ purification (n = 9 mice for whole spleens; n = 5 mice for spleen fraction, n = 10 mice for all others). **j**, Representative flow cytometry illustrating CD103 and LY6C staining of cDC (CD45⁺CD11B⁻CD11c⁺MHCII⁺ cells) from MC38 tumour and spleen. Each data point represents a biological replicate; data are mean ± s.e.m. Data are representative of independent experiments performed at least twice. Data in **h** are from two independent experiments. *P* values were calculated using Welch's two-tailed *t*-test; *P < 0.05. **P < 0.01, ***P < 0.001; exact *P* values are provided in the Source Data.

Extended Data Fig. 7 | See next page for caption.
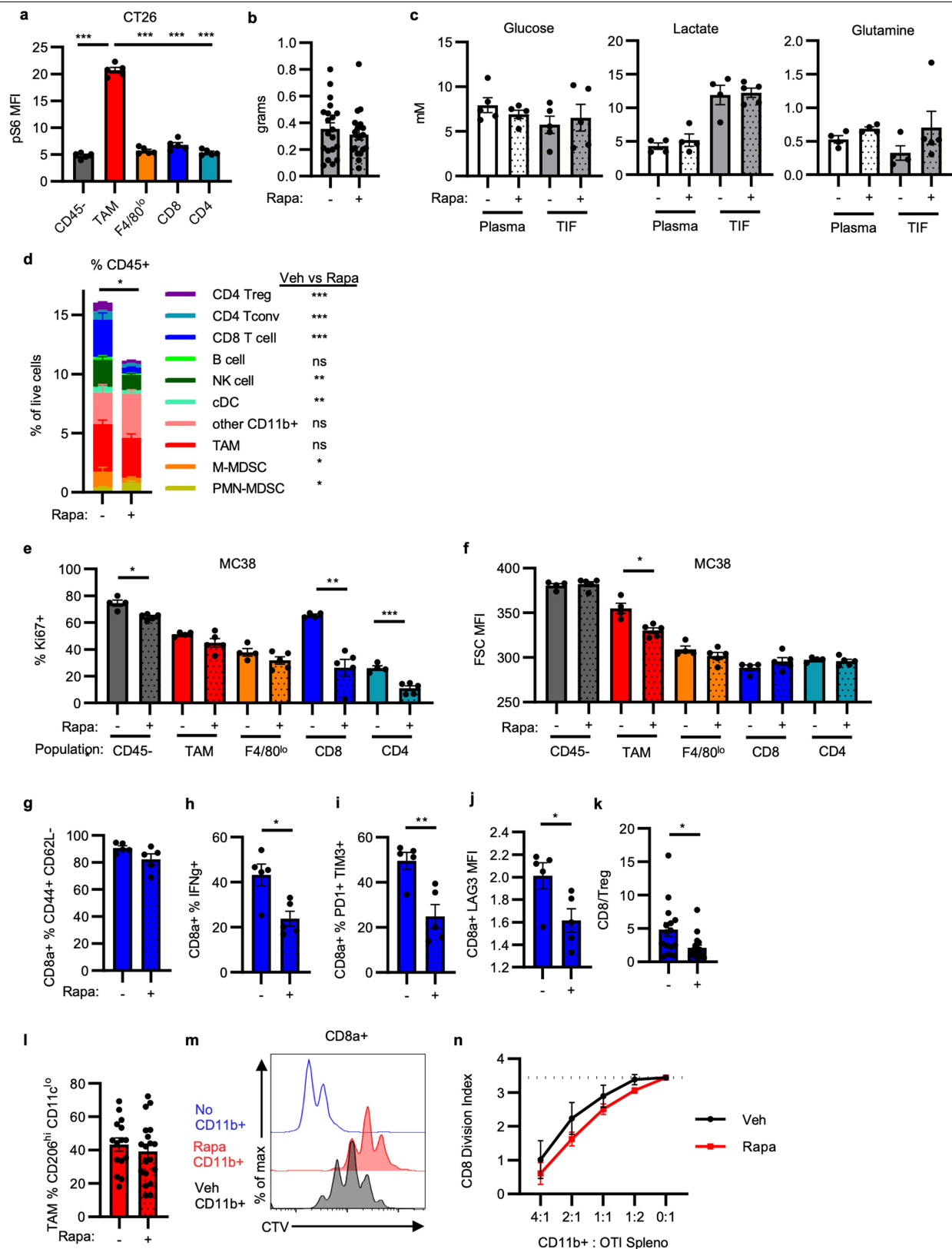
Extended Data Fig. 7 | Supporting data for Fig. 3. a, pS6 levels in CT26 tumour populations ($n = 5$ mice). **b**, MC38 tumour mass at study end-point with rapamycin ($n = 20$ mice for vehicle; $n = 19$ mice for rapamycin). **c**, Metabolite concentrations in tumour interstitial fluid and matched plasma from MC38-tumour-bearing mice treated with rapamycin or vehicle ($n = 5$ mice except for lactate and glutamine plasma and TIF vehicle, $n = 4$ mice). **d**, Immune cell infiltration of MC38 tumours from mice treated with rapamycin or vehicle ($n = 15$ mice for vehicle; $n = 19$ mice for rapamycin). Statistical significance between rapamycin and vehicle treatment for individual populations is indicated. A significant decrease in total CD45$^+$ cell infiltration is noted. **e**, **f**, Flow cytometry quantification of Ki67 positivity (**e**) and cell size (forward scatter, FSC) (**f**) from MC38 tumour populations in mice treated with rapamycin or vehicle ($n = 4$ mice for vehicle; $n = 5$ mice for rapamycin). **g**–**k**, MC38 tumour CD3$^+$CD8A$^+$ T cell phenotypes from rapamycin- or vehicle-treated mice for effector memory phenotype (**g**), ex vivo IFNγ production (**h**), PD1 and TIM3 expression (**i**), LAG3 expression (**j**) ($n = 5$ mice per group) and ratio of CD8$^+$ T cells to CD4$^+$FOXP3$^+$ T$_{reg}$ (**k**) ($n = 15$ mice for vehicle; $n = 19$ mice for rapamycin). **l**, % M2-like TAMs (CD11C^{lo}CD206^{hi}) in MC38 tumours from mice treated with rapamycin or vehicle ($n = 15$ mice for vehicle; $n = 19$ mice for rapamycin). **m**, **n**, Myeloid suppression assay representative histogram of CD8A$^+$ OT-I T cell dilution of CellTrace Violet (CTV), indicative of proliferation (**m**), and quantification of division index (**n**) for MC38 tumour myeloid cells isolated using CD11B$^+$ microbeads from rapamycin- and vehicle-treated mice ($n = 5$ mice per group). Each data point represents a biological replicate; data are mean ± s.e.m. Data in **a**, **e**–**j** are representative of independent experiments performed at least twice; **b**, **d**, **k**–**l** display data merged from four independent experiments. *P* values were calculated using the Brown-Forsythe and Welch ANOVA with Dunnett's T3 for multiple comparison tests (**a**) or Welch's two-tailed *t*-test (**b**–**l**, **n**); *$P < 0.05$. **$P < 0.01$, ***$P < 0.001$; exact *P* values are provided in the Source Data.
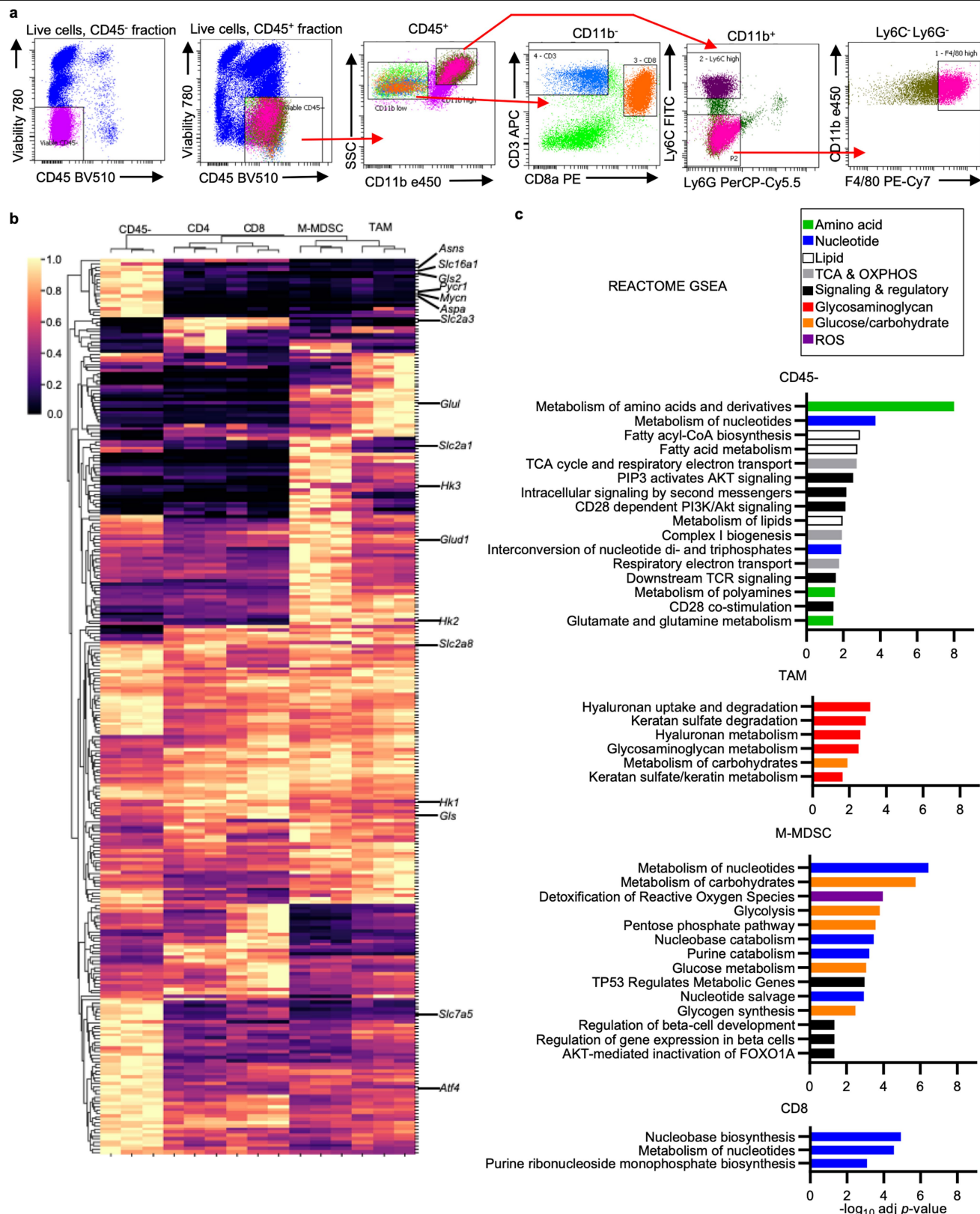
Extended Data Fig. 8 | Metabolic transcriptional signatures of MC38 tumour cell populations. a, Cell sorting scheme of MC38 tumour cell populations used for mRNA transcript analyses. **b**, Clustering analysis heat map of differentially expressed metabolic genes from MC38 tumour cell populations. Selected genes are annotated. **c**, Reactome gene set enrichment analysis for genes most highly expressed in each MC38 tumour population. Significantly enriched gene sets are shown and coloured according to metabolic pathway. OXPHOS, oxidative phosphorylation; TCA, tricarboxylic acid cycle.
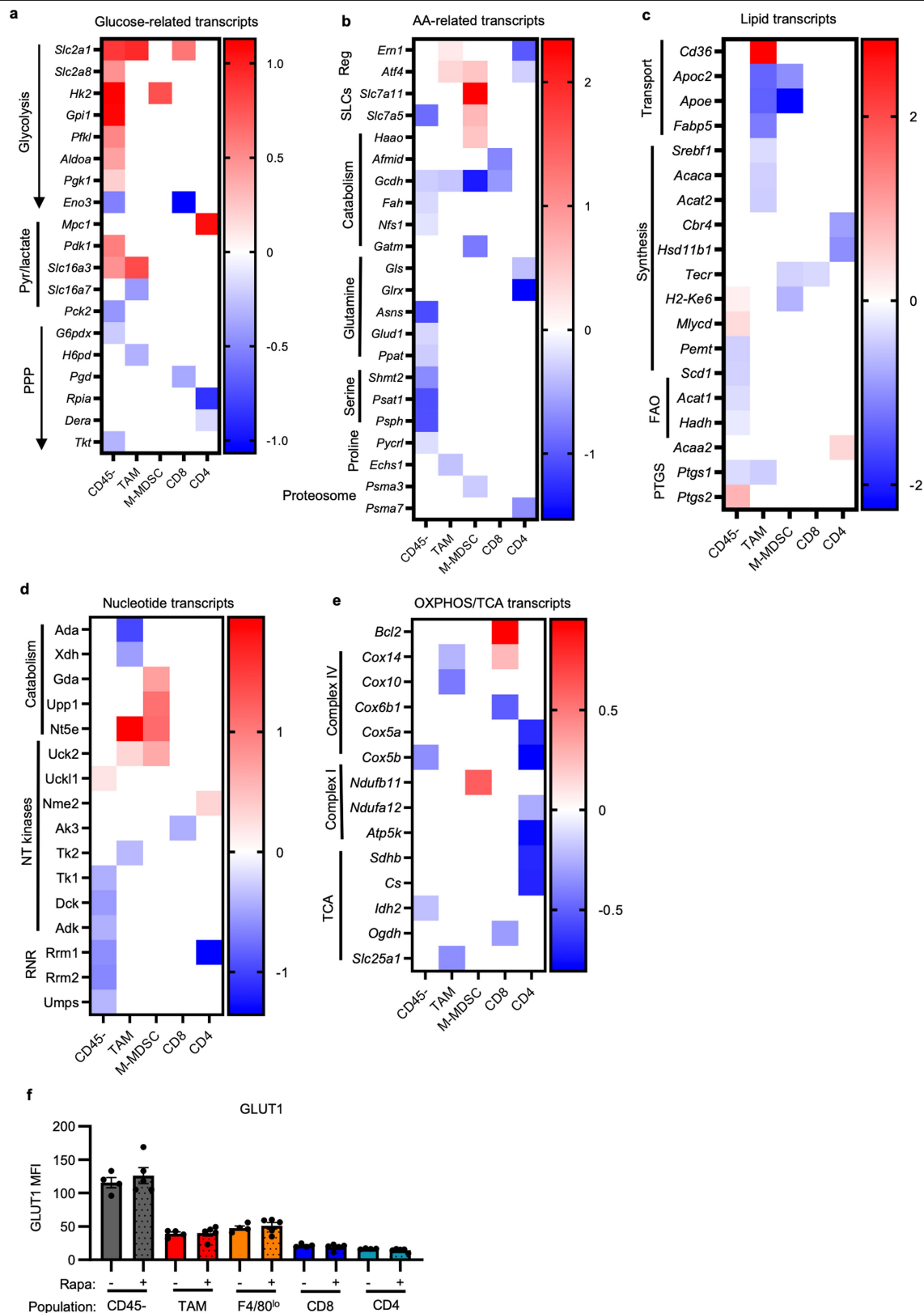
Extended Data Fig. 9 | Effect of rapamycin on metabolic markers of MC38 tumour cell populations. a–e, Heat maps of significantly altered metabolic genes between rapamycin- and vehicle-treated MC38 tumour cell populations for the indicated metabolic pathways. White spaces indicate non-significant changes with rapamycin treatment for that gene and tumour cell population. Genes were grouped and classified manually. (*n* = 3 per group, except *n* = 2 for rapamycin-treated M-MDSCs and CD4⁺ T cells). AA, amino acid; FAO, fatty acid oxidation; NT, nucleotide; PPP, pentose phosphate pathway; PTGS, prostaglandin synthases; reg, regulatory genes; RNR, ribonucleotide reductase; SLCs, solute carrier proteins. **f**, Flow cytometry quantification of GLUT1 expression in MC38 tumour populations from mice treated with rapamycin or vehicle (*n* = 4 mice for vehicle; *n* = 5 mice for rapamycin). Each data point represents a biological replicate; data are mean ± s.e.m; exact *P* values are provided in the Source Data.
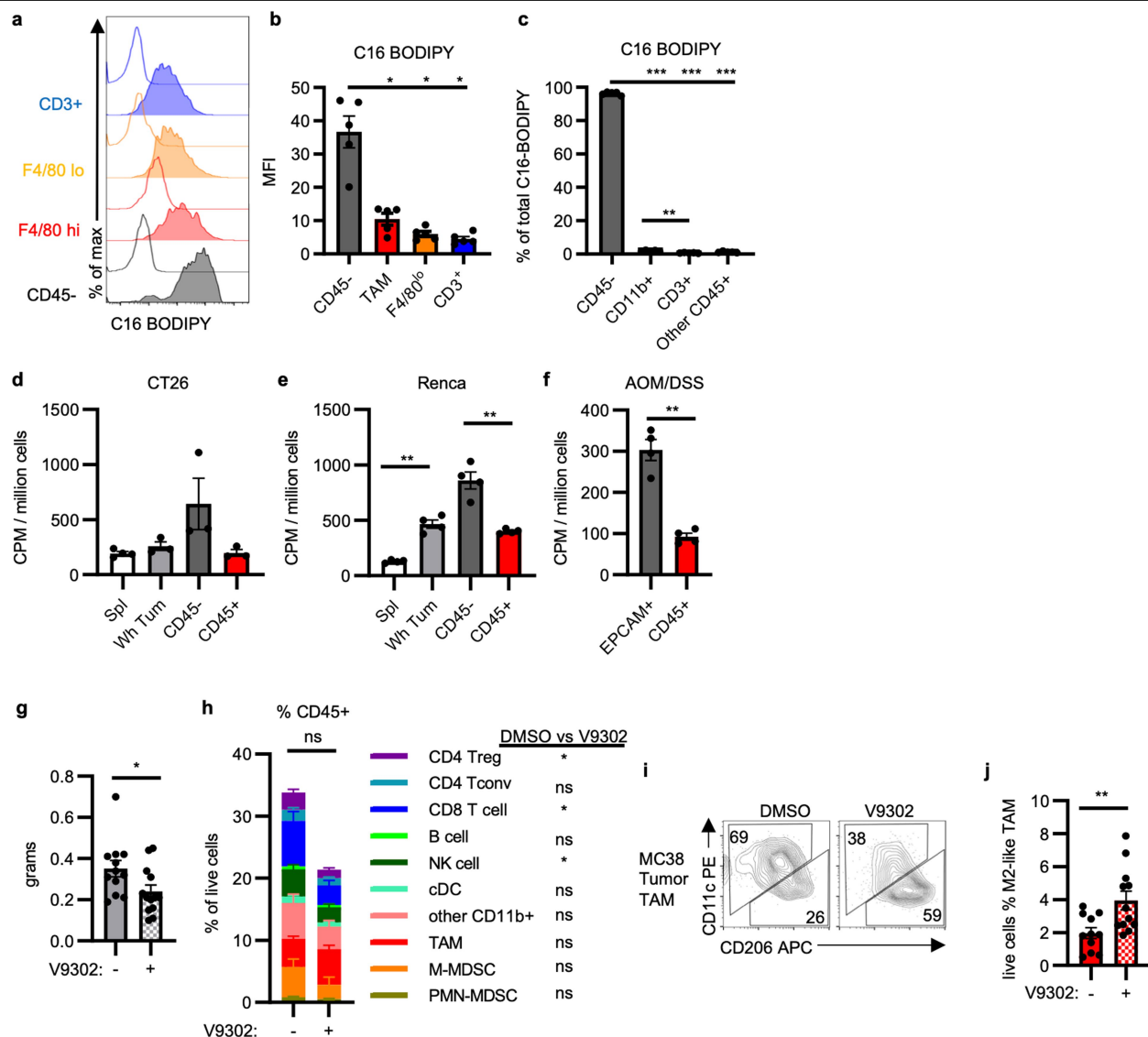
Extended Data Fig. 10 | Supporting data for Fig. 4. a, b, Representative histograms (**a**) and quantification (**b**) for ex vivo staining of C16 BODIPY by indicated MC38 tumour cell populations from tumour single-cell suspensions ($n = 5$ mice). **c,** Per cent contribution to total tumour C16 BODIPY signal from indicated tumour cell populations ($n = 5$ mice). **d–f,** Cellular ^{18}F-Gln avidity in designated tumour cell fractions in CT26 (**d;** $n = 4$ mice for spleen; $n = 3$ mice for tumour) and Renca (**e;** $n = 5$ mice) subcutaneous tumours and AOM/DSS spontaneous tumours (**f;** $n = 4$ mice). **g,** MC38 tumour mass from mice treated with V9302 or DMSO ($n = 13$ mice for V9302; $n = 12$ mice for DMSO). **h,** Immune cell infiltration of MC38 tumours from mice treated with V9302 or DMSO ($n = 13$ mice for V9302; $n = 12$ mice for DMSO). Statistical significance between V9302

and DMSO treatment in distinct populations is indicated. There is no significant change in total CD45$^+$ cell infiltration ($n = 13$ mice for V9302; $n = 12$ mice for DMSO). **i, j,** Representative plot (**i**) and abundance (**j**) of MC38 M2-like TAMs from mice treated with V9302 or DMSO ($n = 13$ mice for V9302; $n = 12$ mice for DMSO). Each data point represents a biological replicate; data are mean ± s.e.m. Data are representative of at least two independent experiments; **g–j** are data combined from two experiments. P values were calculated using the Brown-Forsythe and Welch ANOVA with Dunnett's T3 for multiple comparison tests (**b, c**) or Welch's two-tailed t-test (**d–j**); *$P < 0.05$, **$P < 0.01$, ***$P < 0.001$; exact P values are provided in the Source Data.

Corresponding author(s): W. Kimryn Rathmell
Jeffrey C. Rathmell

Last updated by author(s): Jan 24, 2021

Reporting Summary

Nature Research wishes to improve the reproducibility of the work that we publish. This form provides structure for consistency and transparency in reporting. For further information on Nature Research policies, see our Editorial Policies and the Editorial Policy Checklist.

Statistics

For all statistical analyses, confirm that the following items are present in the figure legend, table legend, main text, or Methods section.

n/a	Confirmed	
☐	☒	The exact sample size (n) for each experimental group/condition, given as a discrete number and unit of measurement
☐	☒	A statement on whether measurements were taken from distinct samples or whether the same sample was measured repeatedly
☐	☒	The statistical test(s) used AND whether they are one- or two-sided *Only common tests should be described solely by name; describe more complex techniques in the Methods section.*
☐	☒	A description of all covariates tested
☐	☒	A description of any assumptions or corrections, such as tests of normality and adjustment for multiple comparisons
☐	☒	A full description of the statistical parameters including central tendency (e.g. means) or other basic estimates (e.g. regression coefficient) AND variation (e.g. standard deviation) or associated estimates of uncertainty (e.g. confidence intervals)
☐	☒	For null hypothesis testing, the test statistic (e.g. F, t, r) with confidence intervals, effect sizes, degrees of freedom and P value noted *Give P values as exact values whenever suitable.*
☐	☒	For Bayesian analysis, information on the choice of priors and Markov chain Monte Carlo settings
☐	☒	For hierarchical and complex designs, identification of the appropriate level for tests and full reporting of outcomes
☐	☒	Estimates of effect sizes (e.g. Cohen's d, Pearson's r), indicating how they were calculated

Our web collection on statistics for biologists contains articles on many of the points above.

Software and code

Policy information about availability of computer code

Data collection
Flow cytometry data were collected using MACSQuantify version 2.1. Extracellular flux data were collected using Seahorse Wave Controller version 2.6. Light microscopy was performed with Olympus cellSens Standard imaging software version 1.17

Data analysis
-PET-CT images were uploaded into Amide (www.sourceforge.com) and volumetric regions-of-interest were drawn around the tumors.
-Flow cytometry data were analyzed using FlowJo v10.7.1
-Extracellular Flux (Seahorse) Data were analyzed in Agilent Wave software version 2.6
-Nanostring data were analyzed using NACHOv1.0.1, an R package for parsing, visualization, quality control, and normalization designed for NanoString nCounter data. Principal component analysis was performed using "FactoMineRv2.3" package in R. Hierarchical clustering of genes in Nanostring studies across samples and genes using default settings with the 'seaborn' package (version v0.11.0) in Python. Based on the hierarchical clustering, we grouped genes and performed gene set enrichment analyses using gProfiler9 with Reactome gene sets compared to all genes. Differentially expressed genes between the rapamycin and vehicle treated samples for each cell type were identified using "edgeR" (version 3.28.1).
-Graphs and statistical tests were generated using GraphPad Prism 9 unless otherwise noted.

For manuscripts utilizing custom algorithms or software that are central to the research but not yet described in published literature, software must be made available to editors and reviewers. We strongly encourage code deposition in a community repository (e.g. GitHub). See the Nature Research guidelines for submitting code & software for further information.

Data

The normalized mRNA transcript data from this experiment has been deposited in Geo and can be accessed at GSE165223 and has been made publicly available.

Field-specific reporting

Please select the one below that is the best fit for your research. If you are not sure, read the appropriate sections before making your selection.

☒ Life sciences   ☐ Behavioural & social sciences   ☐ Ecological, evolutionary & environmental sciences

For a reference copy of the document with all sections, see [nature.com/documents/nr-reporting-summary-flat.pdf](#)

Life sciences study design

All studies must disclose on these points even when the disclosure is negative.

Sample size	Sample sizes were determined by previous experiments and were logistically limited to ~10 mice per experiment for 18F nutrient uptake assays. For smaller effect sizes such as the effect of rapamycin on FDG uptake, data multiple experiments which all independently demonstrated the same phenotypic trends were merged to achieve statistical significance.
Data exclusions	Data were excluded only for systematic quality control purposes. Tumor samples with very low viability (<15%), MC38 tumor samples contaminated with lymph node tissue as suggested by elevated B cell abundance by flow cytometry (rare), FDG uptake samples with raw CPM less than 2-standard deviations above background CPM (rare), and 2 mRNA samples which did not pass quality control were excluded from analysis. For some experiments, biological replicates were merged into a new single biological replicate to ensure sufficient cell numbers. Combined biological replicates causes some figures to have unequal samples sizes across cell populations, treatments, and/or tissues.
Replication	As noted in figure legends, experiments were independently replicated at least twice and demonstrated the same phenotypes unless noted.
Randomization	Mice were randomly assigned to drug treatments immediately prior to treatment initiation, and mice in the same cage were given different treatments.
Blinding	No blinding experiments were involved in this study due to the authors' perceived low likelihood of bias in final readouts.

Reporting for specific materials, systems and methods

We require information from authors about some types of materials, experimental systems and methods used in many studies. Here, indicate whether each material, system or method listed is relevant to your study. If you are not sure if a list item applies to your research, read the appropriate section before selecting a response.

Materials & experimental systems

n/a	Involved in the study
☐	☒ Antibodies
☐	☒ Eukaryotic cell lines
☒	☐ Palaeontology and archaeology
☐	☒ Animals and other organisms
☐	☒ Human research participants
☒	☐ Clinical data
☒	☐ Dual use research of concern

Methods

n/a	Involved in the study
☒	☐ ChIP-seq
☐	☒ Flow cytometry
☒	☐ MRI-based neuroimaging

Antibodies

Antibodies used	Mouse and cross-reactive antibodies: Fc block (1:50, BD 553142), CD45 BV510 (1:1600, 30-F11, Biolegend 103138), B220 e450 (1:400, RA3-6B2, ThermoFisher 48-0452-82), CD11b e450 (1:1600, M1/70, ThermoFisher 48-0112-82), CD11b FITC (1:1600, M1/70, Biolegend 101206), CD8a AF488 (1:1600, 53-6.7, Biolegend 100723), CD8a BV510 (1:600, 53-6.7, BD 563068), Ly6C FITC (1:4000, HK1.4, Biolegend 128006), CD11c PE (1:1000, N418, BioLegend 117308), FOXP3 PE (1:125, FJK-16s, ThermoFisher 12-5773-82), pS6 Ser235/236 PE (1:100, D57.2.2E, Cell Signaling 5316S), CD4 PerCP-Cy5.5 (1:600, RM4-5, BioLegend 100540), Ly6G PerCP-Cy5.5 (1:800, 1A8, BioLegend 127616), F4/80 PE-Cy7 (1:800, BM8, BioLegend 123114), NKp46 PE-Cy7 (1:200, 29A1.4, BioLegend 137618), CD3 PE-Cy7 (1:200, 17A2, BioLegend

100220), CD3 FITC (1:200, 17A2, BioLegend 100204), CD3 APC (1:200 17A2, BioLegend 100236), CD206 APC (1:500, C068C2, BioLegend 141708), GLUT1 AF647 (1:500, EPR3915, Abcam ab195020), EPCAM PE (1:1500, G8.8, BioLegend 118206), Thy1.1 PerCP-Cy5.5 (1:2000, HIS51, ThermoFisher 45-0900-82), CD45 PE (1:1600, 30-F11, ThermoFisher 12-0451-83), Ly6C BV570 (1:400, HK1.4, BioLegend 128030), CD68 BV605 (1:200, FA-11, BioLegend 137021), HK1 AF647 (1:100, EPR10134(B), Abcam ab197864), HK2 AF647 (1:200, EPR20839, Abcam EPR20839), CD71 APC (1:100, RI7217, BioLegend 113820), CD98 PE (1:400, RL388, ThermoFisher 12-0981-81), MHCII I-A/I-E APC (1:4000, M5/114.15.2, BioLegend 107614), CD103 PE-Cy7 (1:200, 2E7, BioLegend 121425), LAG3 e450 (1:100, eBioC9B7W, ThermoFisher 48-2231-82), PD1 PE (1:100, 29F-1A12, BioLegend 135206), TIM3 APC (1:100, RMT3-23, BioLegend 119706), IFNγ APC (1:250, XMG1.2, BioLegend 505810), CD25 e450 (1:500, PD61.5, ThermoFisher 48-0251-82), CD44 PE-Cy7 (1:1000, IM7, BioLegend 103030), and CD62L APC (1:200, MEL-14, ThermoFisher 17-0621-82).
Human antibodies:
CD45 BV421 (1:400, HI30, BioLegend 304032), CD3 APC (1:200, UCHT1, BioLegend 300439), CD11b PerCP-Cy5.5 (1:200, ICRF44, BioLegend 301328), CD14 BV510 (1:200, M5E2, BioLegend 301842), CA9 AF647 (1:200, 303123, R&D Systems FAB2188R-100UG), and Human Fc Block (1:50, BD 564220)

| Validation | Validation information from manufacturer of each antibody:

Mouse Antibody Validation
-CD45 BV510 (1:1600, 30-F11, Biolegend 103138), Positive staining observed on C57BL/6 mouse splenocytes when staining with CD45 (clone 30-F11) Brilliant Violet 510™.
-B220 e450 (1:400, RA3-6B2, ThermoFisher 48-0452-82), This Antibody was verified by Relative expression to ensure that the antibody binds to the antigen stated Staining of C57BL/6 splenocytes with Anti-Mouse CD3e FITC and 0.25 μg and 0.25 μg of Anti-Human/Mouse CD45R (B220) eFluor® 450 results in the expected two single positive populations.
-CD11b e450 (1:1600, M1/70, ThermoFisher 48-0112-82), Positive Staining observed on BALB/c bone marrow cells when using Anti-Mouse CD11b eFluor® 450 (Product # 48-0112-82). Lymphoid cells from the bone marrow do not demonstrate staining.
-CD11b FITC (1:1600, M1/70, Biolegend 101206), Positive staining observed when staining C57B6 bone marrow in comparison to rat IgG2b k FITC isotype control.
-CD8a AF488 (1:1600, 53-6.7, Biolegend 100723), Positive staining observed when staining C57B6 splenocytes in comparison to rat IgG2b k Alexa Fluor® 488 isotype control.
-CD8a BV510 (1:600, 53-6.7, BD 563068), Double positive staining observed when Splenic leucocytes were stained simultaneously with PE Hamster Anti-Mouse CD3e antibody and with CD8a BV510. No double positive events were observed when staining with BD Horizon™ BV510 Rat IgG2a, κ Isotype Control.
-Ly6C FITC (1:4000, HK1.4, Biolegend 128006), Positive staining observed on the myeloid population from C57BL/6 bone marrow cells.
-CD11c PE (1:1000, N418, BioLegend 117308), Double Positive staining observed when C57BL/6 mouse splenocytes were stained with APC anti-mouse I-A/I-E (clone M5/114.15.2) and PE N418 in comparison to single positive staining PE Armenian hamster IgG isotype control. This supports that N418 is staining professional antigen presenting cells.
-FOXP3 PE (1:125, FJK-16s, ThermoFisher 12-5773-82), Positive staining of only the CD4 splenocytes were seen when using the Foxp3/Transcription Factor Staining Buffer Set and protocol. FOXP3 was not detected in the CD8+ stained in the same well.
-pS6 Ser235/236 PE (1:100, D57.2.2E, Cell Signaling 5316S), Positive staining observed in Jurkats. This signal decreased with cocktail of MEK/PI3K inhibitors (LY294002, Wortmannin, and U0126).
-CD4 PerCP-Cy5.5 (1:600, RM4-5, BioLegend 100540), Double positive staining observed on C57BL/6 mouse splenocytes stained with CD3e APC and CD4 (clone RM4-5) PerCP/Cyanine5.5, in comparison to single positive staining with rat IgG2a, kappa PerCP/Cyanine5.5 isotype.
-Ly6G PerCP-Cy5.5 (1:800, 1A8, BioLegend 127616), Positive staining observed with C57BL/6 bone marrow cells stained with 1A8 PerCP/Cyanine5.5.
-F4/80 PE-Cy7 (1:800, BM8, BioLegend 123114), Positive staining observed with Thioglycolate-elicited BALB/c mouse peritoneal macrophages stained with BM8 PE/Cyanine7.
-NKp46 PE-Cy7 (1:200, 29A1.4, BioLegend 137618), Double positive staining observed when C57/BL6 mouse splenocytes were stained with NK1.1 Brilliant Violet 421™ and CD335 (clone 29A1.4) PE/Cyanine7 in comparison to single staining rat IgG2a, κ isotype control PE/Cyanine7. This matches the immunophenotype of NK Cells.
-CD3 PE-Cy7 (1:200, 17A2, BioLegend 100220), Positive staining observed when C57BL/6 splenocytes stained with 17A2 PE/Cyanine7.
-CD3 FITC (1:200, 17A2, BioLegend 100204), Double positive staining observed when C57BL/6 splenocytes stained with 17A2 FITC and CD3e clone 145-2C11 PE.
-CD3 APC (1:200 17A2, BioLegend 100236), Positive staining observed when C57BL/6 mouse splenocytes were stained with CD3 (clone 17A2) APC in comparison to negative staining with rat IgG2b, κ isotype control.
-CD206 APC (1:500, C068C2, BioLegend 141708), Double positive staining observed when staining Thioglycollate-elicited BALB/c peritoneal macrophages with CD107b (Mac-3) PE, and then intracellularly stained with CD206 (clone C068C2) APC. No positive staining observed with rat IgG2a, κ APC isotype control.
-GLUT1 AF647 (1:500, EPR3915, Abcam ab195020), unconjugated antibody has been validated on WT and KO lysates from A549 lung cancer cells.
-EPCAM PE (1:1500, G8.8, BioLegend 118206), Positive staining observed when staining TE-71 (mouse thymic epithelial stromal cell line) with CD326 (clone G8.8) PE. No staining seen with rat IgG2a, κ PE isotype control.
-Thy1.1 PerCP-Cy5.5 (1:2000, HIS51, ThermoFisher 45-0900-82), Positive staining seen on rat thymocytes when stained with Anti-Mouse/Rat CD90-1 (Thy-1-1) PerCP-Cyanine5-5. No staining seen with Mouse IgG2a K Isotype Control PerCP-Cyanine5-5.
-CD45 PE (1:1600, 30-F11, ThermoFisher 12-0451-83), Single positive staining seen with staining C57BL/6 mouse bone marrow cells with TER-119 Monoclonal Antibody, FITC and CD45 Monoclonal Antibody, PE. No PE positive events seen when staining with right Rat IgG2b kappa Isotype Control, PE.
-Ly6C BV570 (1:400, HK1.4, BioLegend 128030), Myeloid cells from C57BL/6 bone marrow cells demonstrated positive staining with Ly-6C (clone HK1.4) Brilliant Violet 570 in comparison to rat IgG2a, κ Brilliant Violet 570™ isotype control.
-CD68 BV605 (1:200, FA-11, BioLegend 137021), thioglycolate-elicited BALB/c macrophages demonstrated positive signal when fixed, permeabilized, and then stained with CD68. No staining was observed with rat IgG2a, κ Brilliant Violet 605™ isotype control.
-HK1 AF647 (1:100, EPR10134(B), Abcam ab197864), unconjugated antibody is knockout validated in HK1 knock out HELA cells in comparison to other cancer cell lines like A549.
-HK2 AF647 (1:200, EPR20839, Abcam EPR20839), unconjugated antibody is knockout validated in wild type and HK2 knock out HCT116s.
-CD71 APC (1:100, RI7217, BioLegend 113820), Double positive staining seen in C57BL/6 mouse bone marrow cells stained with |

Ter-119 PE and CD71 (clone RI7217) APC. This is the expected staining pattern of red blood cells.
-CD98 PE (1:400, RL388, ThermoFisher 12-0981-81), The RL388 antibody has been tested by flow cytometric analysis of activated and resting mouse splenocytes, demonstrating positive straining to conjugated IgG control.
-MHCII I-A/I-E APC (1:4000, M5/114.15.2, BioLegend 107614), Positive staining observed on C57BL/6 mouse splenocytes with anti-mouse I-A/I-E. No staining seen with rat IgG2b, κ APC isotype control.
-CD103 PE-Cy7 (1:200, 2E7, BioLegend 121425), Positive staining observed on C57BL/6 mouse splenocytes were stained with CD3 APC and CD103 (clone 2E7) PE/Cyanine7 (top) in comparison to Armenian hamster PE/Cyanine7 isotype control.
-LAG3 e450 (1:100, eBioC9B7W, ThermoFisher 48-2231-82), Positive staining observed on mouse T cells activated in culture for three days with anti-CD3/CD28 in comparison to Rat IgG1 K Isotype Control eFluor® 450.
-PD1 PE (1:100, 29F-1A12, BioLegend 135206), Double positives observed with Concanavalin A and IL-2 stimulated C57BL/6 splenocytes for 3 days when stained with 29F.1A12 PE and CD3 APC.
-TIM3 APC (1:100, RMT3-23, BioLegend 119706), Positive staining observed when mouse TIM3 transfected cells were stained with this antibody (Tim-3, clone RMT3-23) in comparison to rat IgG2a, κ APC isotype control.
-IFNγ APC (1:250, XMG1.2, BioLegend 505810), Positive staining observed 6 hours after PMA/Ionomycin-stimulation of C57BL/6 mouse splenocytes stained with XMG1.2.
-CD25 e450 (1:500, PD61.5, ThermoFisher 48-0251-82), This antibody was verified by Cell treatment to ensure that the antibody binds to the antigen stated. Positive staining observed on CD8+ splenocytes after two days of IL2 and aCD3/CD28.
-CD44 PE-Cy7 (1:1000, IM7, BioLegend 103030), Positive staining observed on C57BL/6 mouse splenocytes stained with IM7.
-CD62L APC (1:200, MEL-14, ThermoFisher 17-0621-82). Positive staining observed on C57BL/6 mouse splenocytes stained with MEL-14.

Human Antibodies:
-CD45 BV421 (1:400, HI30, BioLegend 304032), Positive staining observed when Human peripheral blood lymphocytes were stained with CD45 (clone HI30) Brilliant Violet 421™. No Positive staining seen when staining same cells with mouse IgG1, κ Brilliant Violet 421™ isotype control.
-CD3 APC (1:200, UCHT1, BioLegend 300439), Positive staining observed when staining Human peripheral blood lymphocytes stained with UCHT1 APC.
-CD11b PerCP-Cy5.5 (1:200, ICRF44, BioLegend 301328), Positive staining observed on Human peripheral blood mononuclear cells were with CD11b (clone ICRF44) PerCP/Cyanine5.5 (top). No positive events seen with mouse IgG1, kapp PerCP/Cyanine5.5 isotype control.
-CD14 BV510 (1:200, M5E2, BioLegend 301842), Positive staining observed when Human peripheral blood monocytes were stained with CD14 (clone M5E2) Brilliant Violet 510™.
-CA9 AF647 (1:200, 303123, R&D Systems FAB2188R-100UG), Antibody tested for flow cytometry on HeLa cells. s. This antibody is specific based on direct ELISAs performed by manufacturer. This antibody clone does not cross-react with recombinant mouse (rm) CA9 or with rhCA1, 2, 3, 4, 5A, 6, 7, 8, 10, 12, 13, or 14.

Eukaryotic cell lines

Policy information about cell lines

Cell line source(s)	MC38 and CT26 were obtained from Barbara Fingleton lab at Vanderbilt. Renca was obtained from ATCC.
Authentication	Cell lines were previously validated by STR profiling.
Mycoplasma contamination	All cell lines tested negative for mycoplasma contamination
Commonly misidentified lines (See ICLAC register)	None

Animals and other organisms

Policy information about studies involving animals; ARRIVE guidelines recommended for reporting animal research

Laboratory animals	C57BL/6J (000664), BALB/cJ (000651), Rag1 KO (002216) and OTI transgenic (003831) mice were obtained from the Jackson Laboratory. PyMT GEMM mice were bred by crossing male transgenic mice expressing the polyoma virus middle T antigen (PyMT) oncoprotein under the MMTV-LTR (Jackson Laboratory 022974) with wildtype females on a similar B6/FVB mixed background. The GEMM mice were from a colony in which all mice expressed two Vhl alleles in which exon 1 is flanked by loxP sites (Jackson Laboratory 012933) but did not express a Cre transgene and were thus effectively wildtype. For injectable tumor models, 8-20 week old male and female mice were used. Mice were on 12 hour light/dark cycles which coincided with daylight in Nashville, TN. The mouse housing facility was maintained at 68-76°F and 30-70% humidity.
Wild animals	None
Field-collected samples	None
Ethics oversight	Vanderbilt University Medical Center Institutional Animal Care and Use Committee.

Note that full information on the approval of the study protocol must also be provided in the manuscript.

Human research participants

Population characteristics	Samples from recently resected tumor and matched PBMCs were analyzed. Patient characteristics are provided in Supplemental Information Table 1.
Recruitment	Patients sign a separate consent allowing tissue studies to be conducted on resected tumor and PBMC. Patients were treated at Vanderbilt University Medical Center and were uniformly recruited at the time leading up to surgery. The authors do not believe any selection biases are evident in patient recruitment which would make results non-representative.
Ethics oversight	Vanderbilt University Medical Center IRB

Note that full information on the approval of the study protocol must also be provided in the manuscript.

Flow Cytometry

Plots

Confirm that:

☒ The axis labels state the marker and fluorochrome used (e.g. CD4-FITC).

☒ The axis scales are clearly visible. Include numbers along axes only for bottom left plot of group (a 'group' is an analysis of identical markers).

☒ All plots are contour plots with outliers or pseudocolor plots.

☒ A numerical value for number of cells or percentage (with statistics) is provided.

Methodology

Sample preparation	Single cell suspensions obtained from tumors and spleens were incubated in Fc block for 10min at room temp, stained for surface markers for 15min at room temp, washed with FACS buffer (PBS +2% FBS) once, and resuspended in FACS buffer for analysis on a Miltenyi MACSQuant Analyzer 10 or 16. For intracellular staining, the eBioscience™ Foxp3/transcription factor staining buffer kit (Fisher 00-5523-00) was used. For intracellular cytokine staining, tumor single cell suspensions were incubated for 4hr at 37°C 5% CO2 in supplemented RPMI with PMA (50ng/mL, Sigma Aldrich P8139-1MG), ionomycin (750ng/mL, Sigma Aldrich I0634-1MG), and GolgiPlug (1:1000, BD 555029), and processed using the BD Cytofix/Cytoperm™ Fixation and Permeabilization Solution (ThermoFisher BDB554722). Surface staining was performed as described above, cells were fix/permed for 20min at 4°C, and then stained for intracellular markers for at least 30min at 4°C. Ghost Dye Red 780 viability dye (1:4000, Cell Signaling 18452S) was used identically to surface antibodies.
Instrument	Miltenyi MACSquantAnalyzer 10 or 16
Software	FlowJo version 10.7.1
Cell population abundance	Purity, viability, and yield of all magnetic bead sorted cells were measured by flow cytometry and trypan staining. Purity of flow-sorted cells for mRNA analysis was confirmed by transcript levels of cell identification markers.
Gating strategy	Singlets were gated using FSC-Area vs FSC-Height. Then, dead cells were excluded using viability dye 780 vs FSC. Additional low FSC / low SSC debris were excluded by gating on FSC and SSC compared to splenocytes or PBMC as highly viable lymphocyte controls. From this total live cell gate, CD45+ immune cells were then gated versus CD45- cells. CD45- cells were additionally gated on high FSC and SSC before subsequent analysis to gate on cancer cells more specifically. For more specific gates, see Extended Data Figure 5h and 8a.

☒ Tick this box to confirm that a figure exemplifying the gating strategy is provided in the Supplementary Information.